Tectonophysics 671 (2016) 76–94

Contents lists available at ScienceDirect

Tectonophysics

journal homepage: www.elsevier.com/locate/tecto

Tectonic models for the Patagonian orogenic curve (southernmost Andes): An appraisal based on analog experiments from the Fuegian thrust–fold belt

Pablo J. Torres Carbonell [a,*], Cecilia Guzmán [b], Daniel Yagupsky [b], Luis V. Dimieri [c]

[a] Centro Austral de Investigaciones Científicas (CADIC-CONICET), Bernardo Houssay, 200, 9410 Ushuaia, Tierra del Fuego, Argentina
[b] Laboratorio de Modelado Geológico, Instituto de Estudios Andinos "Don Pablo Groeber", Departamento de Ciencias Geológicas, FCEN-UBA, C1428EHA Ciudad Universitaria, Pabellón 2, Argentina
[c] Instituto Geológico del Sur (INGEOSUR-CONICET), Departamento de Geología, Universidad Nacional del Sur, San Juan 670, 8000 Bahía Blanca, Buenos Aires, Argentina

ARTICLE INFO

Article history:
Received 3 July 2015
Received in revised form 17 December 2015
Accepted 10 January 2016
Available online 27 January 2016

Keywords:
Analog modeling
Patagonian orocline
Fuegian Andes
Rotational backstop
Basement promontory
Buttressing

ABSTRACT

Tectonic models for the evolution of the Patagonian orogenic curve were evaluated using analog experiments that considered either a rotational or a non-rotational orogenic backstop, combined with a basement promontory on the foreland cratonic margin. Five different kinematic configurations were used, aiming to evaluate the influence of the Río Chico Arc as a rigid obstacle on the evolution of the Fuegian thrust–fold belt. Rotations, strains and displacement fields obtained from each analog experiment were compared with the structural geology known from the Fuegian thrust–fold belt, in order to appraise the tectonic models that are more consistent with the natural structure. The push of a counterclockwise rotational backstop, combined with the buttressing effect of a foreland promontory, seem of major importance in controlling the final structure and map-view shape of the thrust wedge.

1. Introduction

The Fuegian thrust–fold belt constitutes the orogenic front of the southernmost Andes in Tierra del Fuego, where they form the eastern part of an orogenic curve changing strike from N–S to E–W in an arc-distance of almost 500 km (Fig. 1). The origin of this curve, named Patagonian Orocline by Carey (1958) (we use here the term Patagonian curve), has been considerably disputed. While initial studies revealed that part of the orogen has been apparently bent in a counterclockwise (CCW) motion of about 90° (Burns et al., 1980; Cunningham et al., 1991; Dalziel et al., 1973), recent ones argued that bending, if occurred, did not affect foreland strata younger than 50 Ma (Maffione et al., 2010), or only affected discrete portions of the Patagonian curve due to non-coaxial deformation (Poblete et al., 2014). These recent paleomagnetic studies appear to support a primary curve origin (cf. Marshak, 2004) for the thrust–fold belt, which contains curved thrusts as young as early Miocene in Tierra del Fuego. On the other hand, taking into account CCW rotations for the outer arc of the Patagonian curve (cf. Poblete et al., 2013), a model can be put forward where a rotating backstop of older rocks in the core of the orogen bulldoze the foreland basin sediments (Ghiglione and Cristallini, 2007; Torres Carbonell et al., 2014). Different patterns of rotations could result from such a scenario.

An additional aspect considering this latter framework is that during orogenesis the thrust–fold belt collided with the rigid foreland, especially in the Fuegian limb of the orogenic curve. It has recently been proposed that the foreland cratonic margin, with an irregular shape, may have exerted a buttressing effect on the thrust–fold belt, thus conditioning its curved configuration and its tectonic evolution (Torres Carbonell et al., 2013a). This aspect becomes even more important taking into account the Late Cretaceous to Miocene underthrusting of the cratonic slab as a fundamental part of the Fuegian Andes development (Klepeis et al., 2010; Torres Carbonell and Dimieri, 2013). This idea is also supported by seismic evidence showing the control of the foreland basement topography on the location of frontal structures of the thrust–fold belt (Torres Carbonell et al., 2013a).

The effects of a rotational vs. an originally curved backstop have been already tested with analog models, finding that both configurations can cause an arcuate sand wedge similar to the Patagonian curve. The models performed reveal diverse displacement fields, variable shortenings along the arc, and changing amounts of thrusting vs. strike-slip faulting (Ghiglione and Cristallini, 2007). However, recent work in the Tierra del Fuego has shown features of the thrust–fold belt that were not accounted for in those previous models, particularly the concave-to-the-north recess along the Fuegian thrust–fold belt (Península Mitre Recess), whose eastern termination reveals a turn

* Corresponding author.
E-mail addresses: torrescarbonell@cadic-conicet.gob.ar (P.J. Torres Carbonell), ceciliagguzman@hotmail.com (C. Guzmán), yagdaniel@gmail.com (D. Yagupsky), ldimieri@uns.edu.ar (L.V. Dimieri).

http://dx.doi.org/10.1016/j.tecto.2016.01.020
0040-1951/

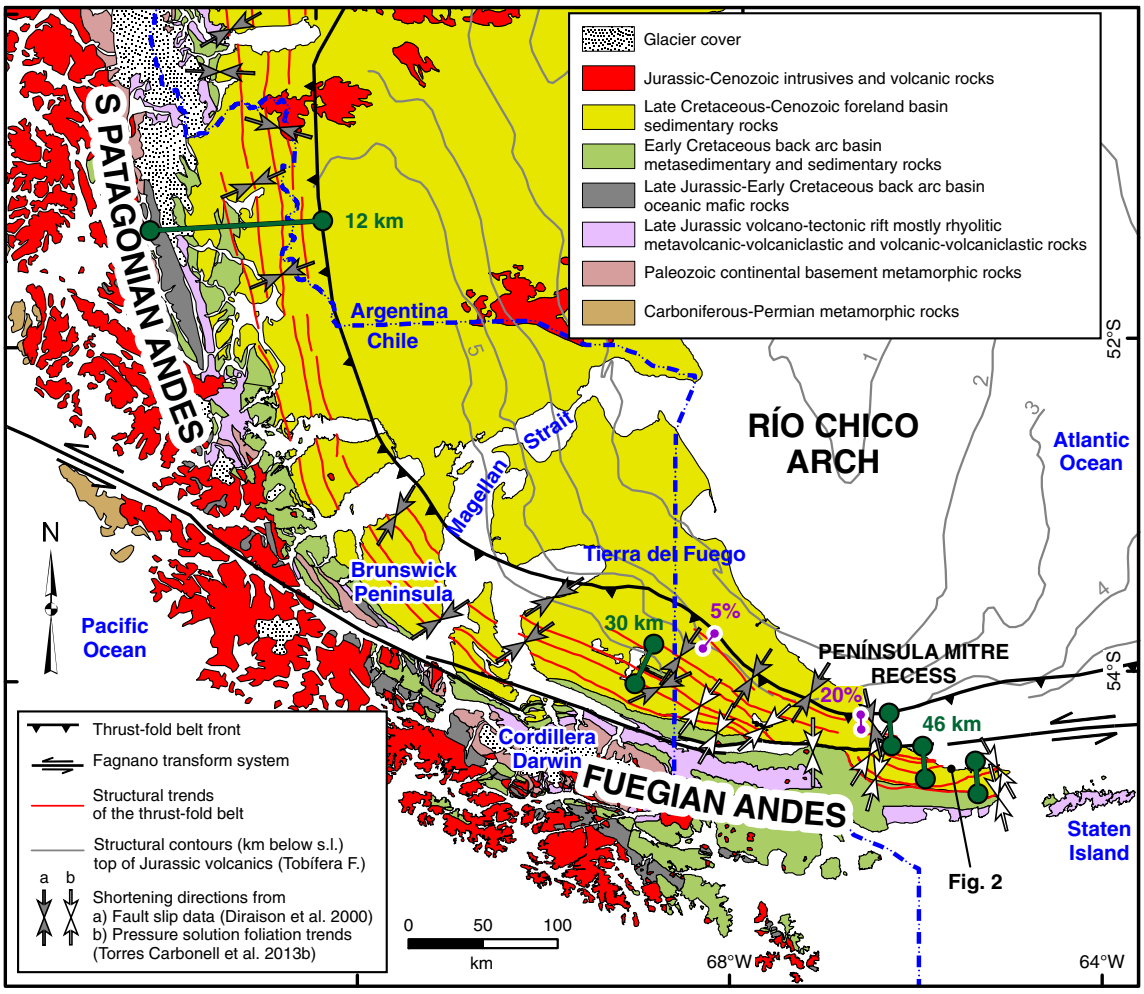

Fig. 1. Geologic map of the Patagonian curve, compiled from Olivero and Malumián (2008), Panza et al. (2002), SERNAGEOMIN (2003), and Klepeis et al. (2010). Green bars indicate location of shortening estimations for the foreland thrust–fold belt (Cretaceous–Cenozoic cover), from Fosdick et al. (2011) in the South Patagonian Andes, Alvarez-Marrón et al. (1993) in the Chilean part of Tierra del Fuego, and Torres Carbonell and Dimieri (2013) in the Península Mitre Recess. Shortening percentages for the frontal portion of the Fuegian thrust–fold belt are indicated in magenta, from Torres Carbonell et al. (2013a). (For interpretation of the references to color in this figure legend, the reader is referred to the web version of this article.)

towards SW–NE structural trends (Fig. 1) (Torres Carbonell et al., 2013a). The shortening directions change along the recess, keeping perpendicularity with local structures, and are therefore NW–SE oriented at the eastern limb of the recess (Torres Carbonell et al., 2013a,b). There is also a lateral variation in shortening magnitudes obtained from structural cross-sections, which indicate significantly higher percentages of shortening in the axis of the recess (Fig. 1) (Torres Carbonell et al., 2013a).

In this work we used analogue modeling to test different structural configurations resembling alternative hypotheses for the evolution of the Patagonian curve, either with a rotational or a non-rotational orogenic backstop, considering the fundamental role of the foreland cratonic margin geometry in the evolution of the Fuegian thrust–fold belt. The results of the analog experiments contribute to the appraisal of different tectonic models for this portion of the Andes, by means of evaluating the consistence of these results with the structural data from the Fuegian thrust–fold belt.

2. Geologic background of the Fuegian Andes

The Fuegian Andes extend with a WNW–ESE regional trend from the Magellan Strait to Staten Island, forming the eastern limb (or Fuegian limb) of the Patagonian curve (Fig. 1). Since the Oligocene they constitute part of the NW Scotia Arc, and are connected to the east with the North Scotia Ridge. For our purposes, we will describe the prior history of the Fuegian Andes starting from the Late Jurassic continental stretching in SW Gondwana (South America) that led to a volcano-tectonic rift, which was associated with deposition of volcanic and volcaniclastic rocks on Paleozoic continental crust (Calderón et al., 2007; Wilson, 1991). Stretching continued until the Early Cretaceous, causing the local creation of oceanic floor in a back arc basin called Rocas Verdes Basin (Calderón et al., 2007; Mukasa and Dalziel, 1996). Marginal marine to arc-derived sediments filled this basin until the Albian (Fildani and Hessler, 2005; Olivero and Martinioni, 2001).

The Rocas Verdes Basin rimmed SW Gondwana for more than 1500 km, and was connected southeastward with the Weddell Sea (Dalziel et al., 2013a). The west-SW border of the Rocas Verdes Basin was a volcanic arc rooted on ensialic crust (Dalziel, 1986), probably connected to the south with the Antarctic Peninsula (Barker, 2001; Dalziel et al., 2013a).

As revealed by structural maps (Biddle et al., 1986; Yrigoyen, 1989), the cratonic margin of the Rocas Verdes Basin has a general SSE trend in the NW part of the basin, but toward the east this margin projects southwards for about 300 km forming the Río Chico (or Dungeness) Arch (Fig. 1). The promontory's southern tip is best defined below its 1.5 km depth structural contour. The Río Chico Arch plunges toward the south, with a topography controlled by Late Jurassic-Early Cretaceous normal faults that bound grabens and hemigrabens created during the

Jurassic continental stretching, and reactivated during Cretaceous–Paleogene subsidence (Galeazzi, 1998; Ghiglione et al., 2010; Robbiano et al., 1996).

The Rocas Verdes Basin closed in the Late Cretaceous due to increased westward movement of the South America plate (Dalziel, 1986). In Tierra del Fuego, the history of closure involved obduction of the oceanic floor and underthrusting of the South American cratonic margin, and further collision of the magmatic arc with the cratonic margin (Klepeis et al., 2010; Nelson et al., 1980). High-grade metamorphic conditions (upper-amphibolite facies) in the middle crust were reached during basin closure and initial buildup of the Fuegian Andes (Kohn et al., 1993; Nelson et al., 1980). The back arc continental basement, as well as Jurassic granites, Upper Jurassic volcanics, and the oceanic floor and sedimentary fill of the Rocas Verdes Basin were all affected by N- and NE-vergent (present day orientation) folds and ductile thrusts associated with basin closure (Klepeis et al., 2010; Nelson et al., 1980). Away from the higher-metamorphic grade zone of Cordillera Darwin (Fig. 1), greenschist or lower facies regional metamorphism accompanied the deformation associated with foreland directed simple shear (Bruhn, 1979; Tanner and Macdonald, 1982; Torres Carbonell and Dimieri, 2013).

Further contraction from the Late Cretaceous to the early Neogene produced large scale thrusting of the continental margin, with deformation transferred to shallower levels in the crust affecting a coeval foreland basin (Austral or Magallanes Basin) (Torres Carbonell and Dimieri, 2013). This gave birth to the Fuegian thrust–fold belt, with major detachments at Lower Cretaceous and Paleocene horizons (Zanella et al., 2014; Torres Carbonell et al., 2011).

The initial thrust wedge affected Cretaceous sedimentary rocks under low to very-low grade metamorphic conditions, associated with development of tectonic disjunctive foliations formed by pressure-solution. The regional trends of these foliations reveal the early formation of a concave-to-the-north map-view curve, called Península Mitre Recess (Fig. 1) (Torres Carbonell et al., 2013b). The recess continued to grow as younger thrusts where emplaced in the thrust–fold belt until the Early Miocene, as recorded by the youngest syntectonic angular and progressive unconformities in lower Miocene beds (Ghiglione et al., 2010; Ponce et al., 2008; Torres Carbonell et al., 2013a).

Measurements from balanced cross-sections and from the analysis of depth-converted seismic sections in the frontal thrust–fold belt indicate that shortening increased toward the apex of the Península Mitre Recess (Fig. 1). Accordingly, structural geometries at this site are more complex, with closer folds than at the western limb of the recess (Torres Carbonell et al., 2013a). This is revealed not only at the thrust front, but also at inner sectors of the recess, where a cross-section of the apex reveals a very complex structural style in the Upper Cretaceous–Cenozoic deformed strata, including north- and south-vergent structures, and out-of-sequence thrusts, formed during several structural stages and with an overall shortening of at least 46 km (Fig. 1) (Torres Carbonell and Dimieri, 2013; Torres Carbonell et al., 2011). At the region of maximum curvature in map-view, the thrust–fold belt is overprinted by gentle N–S oriented folds (Fig. 2A) (Torres Carbonell et al., 2011), consistent with some recently obtained post-middle Eocene paleostress tensors from fault slip data in the same region, which indicate compression parallel to the structural trends (Maestro

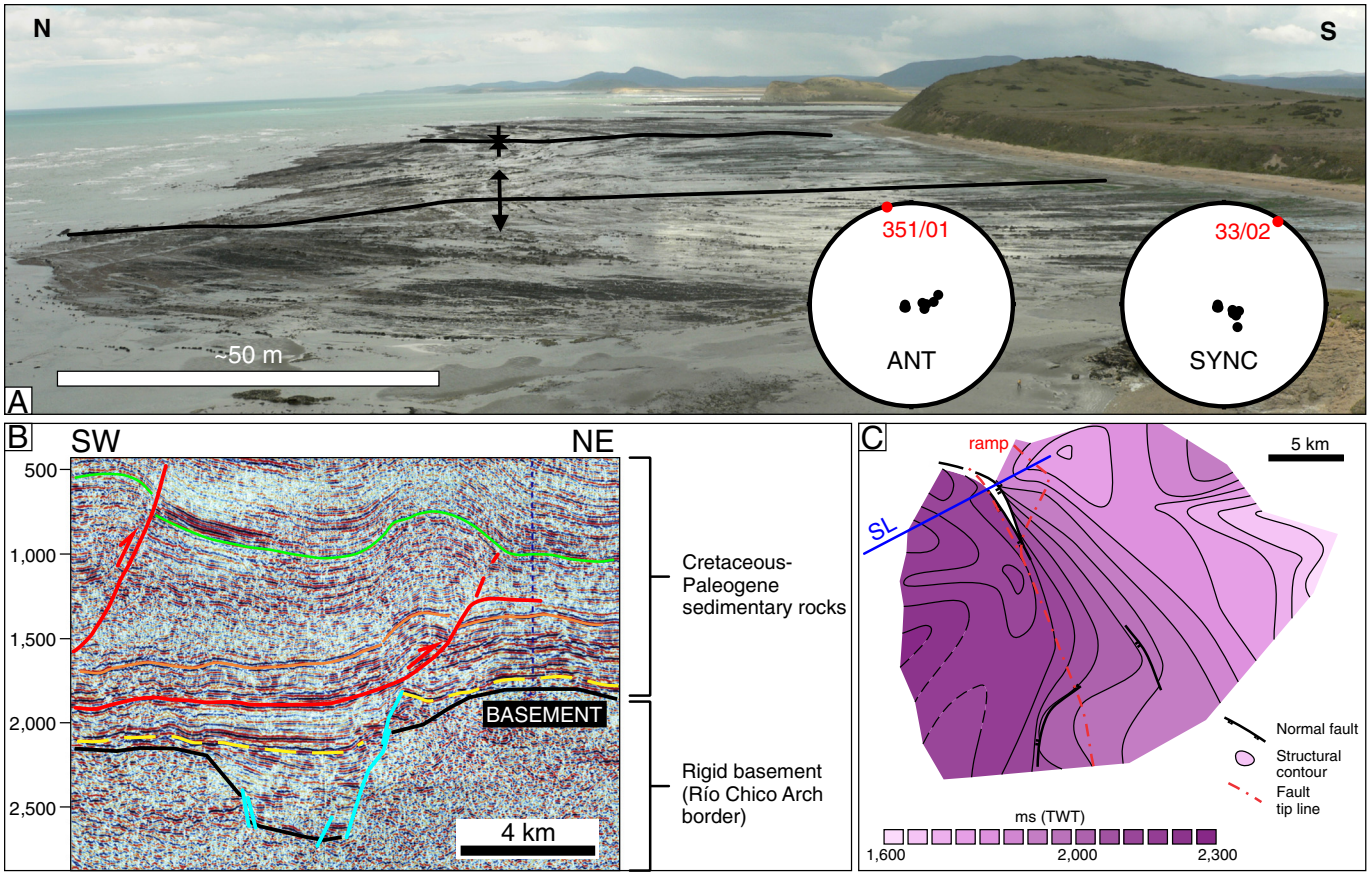

Fig. 2. A. N–S oriented folds in the apex of the Península Mitre Recess (location in Fig. 1). Stereographic diagrams show poles to bedding planes in the anticline (ANT) and syncline (SYNC), and calculated beta axes in red. B. Seismic reflection line of the thrust–fold belt front showing the location of the leading thrust above a basement scarp in the SW border of the Río Chico Arch (section located nearby the site of Fig. 1 where the 5% shortening bar is shown). The scarp is genetically related to normal faults (cyan colored) formed prior to contraction. Modified from Torres Carbonell et al. (2013a). C. Structural map of the horizon shown as a dashed yellow line in Fig. 2B (also affected by the normal faults), with location of the seismic line (SL). Note the rough coincidence between the tip line of the leading thrust and the structural contours that define the border of the Río Chico Arch below this horizon.
Modified from Torres Carbonell et al. (2013a). (For interpretation of the references to color in this figure legend, the reader is referred to the web version of this article.)

et al., 2015). In comparison, the structural style at the western limb of the recess (the only one exposed onshore), shows northeast-vergent thrust-sheets and related folds, continuous along strike for many kilometers, which at the frontal 50 km of the belt are open to gentle, large-wavelength folds (Alvarez-Marrón et al., 1993; Zanella et al., 2014). Calculated shortenings for that part of the thrust–fold belt range between 30 and 35 km (Fig. 1) (Alvarez-Marrón et al., 1993; Kley et al., 1999; see Torres Carbonell and Dimieri, 2013 for an analysis of reported shortenings).

After contraction ceased, a strike-slip faulting regime, associated with the development of the seismogenic Fagnano (Magallanes) transform system (Fig. 1) (Lodolo et al., 2003), controlled the tectonic history of Tierra del Fuego since the Late Miocene (Torres Carbonell et al., 2008a). Birth of the Fagnano transform system is probably related to the onset of the northern transform boundary of the Scotia Plate, which runs along the North Scotia Ridge since the Late Miocene (~11 Ma) (Barker, 2001; Dalziel et al., 2013b). The main effect of this strike-slip deformation in the Fuegian Andes is the ~50 km left-lateral offset of the previous contractional structures along a ~10 km wide, roughly E-W striking deformation zone (Torres Carbonell et al., 2008a). The effect of this fault zone on rocks older than the Quaternary is rarely exposed. However, everywhere they post-date the Late Cretaceous–early Neogene thrust–fold belt structures (Klepeis, 1994; Torres Carbonell et al., 2008a, 2011).

2.1. Tectonic models for the orogenic curve

The original interpretation of the Patagonian curve as an orocline (Carey, 1958) has been in part supported by paleomagnetic data from the southernmost Andean belt (Burns et al., 1980; Cunningham et al., 1991; Dalziel et al., 1973; Poblete et al., 2013; Rapalini, 2007). Some of the paleomagnetic data, however, are not constrained by present-day standards and thus the rotational origin of the Patagonian curve remains uncertain (Rapalini, 2007). Nevertheless, based on the apparently consistent distribution of paleomagnetic declinations that reveal variable amounts of CCW rotations, many proposed models for the origin of the curve involve bending.

Burns et al. (1980) first explained the closure of the Rocas Verdes basin by CCW rotation of the pacific-side magmatic arc during the Late Cretaceous. A similar model was later developed by Kraemer (2003), who proposed that rotation continued through the Cenozoic until the Miocene, stopping when thrust–fold belt tectonics ceased. Cunningham (1993) explained the evolution of the Patagonian curve within a context of regional E–W left-lateral strike-slip tectonics since 120 Ma to the late Neogene, which caused the Southernmost Andes–Antarctic Peninsula continental belt to be dissected by numerous left-lateral strike-slip faults, ultimately causing continental separation and creation of Drake Passage. The Fuegian Andes, according to this interpretation, were affected by transpression and pure strike-slip faulting. The orogen was separated into blocks bounded by strike-slip faults, each rotated in a CCW sense. Even if attractive, this model is not consistent with structural data from the Fuegian Andes obtained after Cunningham's model. These data include: evidence of major thrust-related contraction both in the internal orogenic wedge (Klepeis et al., 2010; Torres Carbonell and Dimieri, 2013; Cao et al., 2015) and in the thrust–fold belt (Torres Carbonell et al., 2011; Zanella et al., 2014); and conspicuous evidence indicating that the major strike-slip faults are younger than the contractional structures (Torres Carbonell et al., 2008a,b, 2011; Klepeis et al., 2010), and most probably related to the initiation of the transform boundary between the South American and Scotia plates during the Miocene (Fig. 3) (Barker, 2001; Dalziel et al., 2013a,b).

A similar tectonic model involving transpression was put forward by Diraison et al. (2000). This model also assumed that strike-slip tectonics dominated the deformation style of the Fuegian Andes and Patagonian curve since its Late Cretaceous origin, in coincidence with the model presented by Cunningham (1993). The structural data presented by Diraison et al. (2000) consists on fault slip data analyzed for bulk strain estimations. However, no data on the relative age of faulting is presented in that work, and all faults are assumed to pertain to a single phase of Late Cretaceous–Cenozoic age. This span is clearly large enough to consider more than one faulting phase (Maestro et al., 2015). Thus, analogous to Cunningham's proposal, the model from Diraison et al. (2000) is weakened by the same younger structural dataset obtained in the region, mentioned above, which indicates contraction followed by strike-slip faulting.

Diraison et al. (2000) also presented a lithospheric-scale analog model involving an oceanic plate subducted beneath a continental corner, which acted as an area of transition from frontal subduction,

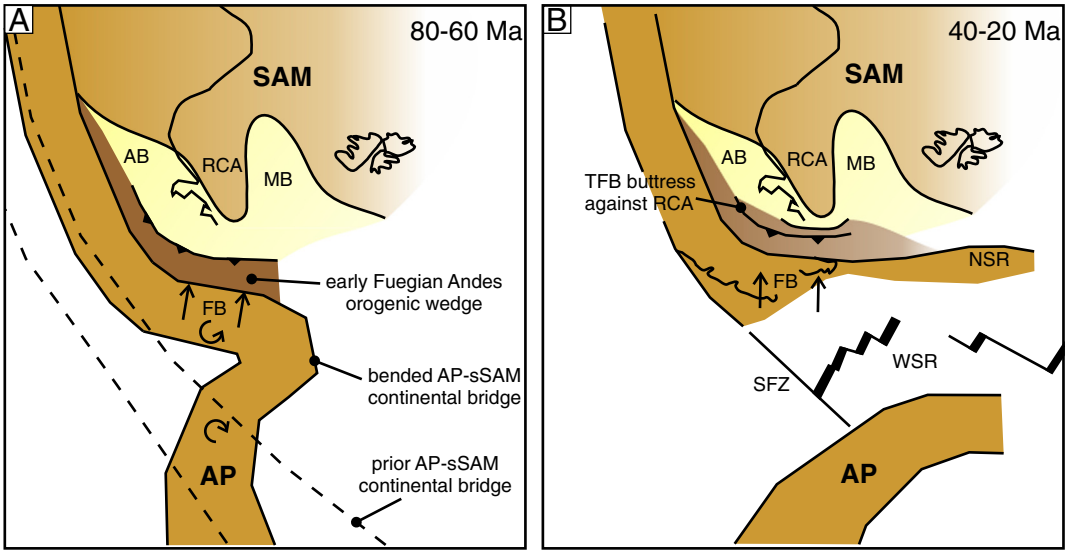

Fig. 3. Schematic diagrams depicting the Late Cretaceous–Cenozoic tectonic evolution of the Fuegian Andes prior to the development of the Fagnano Transform System, according to Torres Carbonell et al. (2014). Continental crust is brown, the foreland basin system is light yellow, and oceanic domains are white. Bending of the southernmost South America (sSAM)-Antarctic Peninsula (AP) continental bridge, and further separation during opening of the West Scotia Ridge (WSR), caused movement of the Fuegian backstop (FB) against the southern cratonic margin of the South American plate (SAM). Collision of the orogenic wedge against the Rio Chico Arch promontory (RCA) that separates the Austral and Malvinas basins (AB and MB), forced the curvature of the Fuegian thrust–fold belt (TFB). NSR: North Scotia Ridge, SFZ: Shackleton fracture zone. (For interpretation of the references to color in this figure legend, the reader is referred to the web version of this article.)

to left-lateral strike-slip. However, the model concentrated on the Neogene deformation of southernmost South America, when the Patagonian curve already existed, therefore it doesn't address the main topic of our discussion (i.e. the tectonic models for the Patagonia curve).

On the other hand, a model for a primary curve was presented by Ghiglione and Cristallini (2007), who used analog models to test the resulting effects of a concave backstop pushing the sedimentary cover toward the foreland. The curved indenter was forced into the sand fill resembling the push of a curved orogen (of Late Cretaceous age) toward the Cenozoic foreland basin; experiments involved both a fixed and a CCW rotational backstop. The models successfully reproduced the Patagonian curve, and the authors considered that the best model was one where indentation occurred in two phases: the first one highly oblique to the Fuegian segment of the orogen (NE directed motion), and the second one highly oblique to the Patagonian segment and parallel to the Fuegian limb (ESE directed motion). This experiment resulted in ESE structural trends in the Fuegian segment, i.e. mostly parallel to the backstop.

Recent paleomagnetic results from foreland basin sedimentary rocks reveal that no vertical axis rotations took place in the eastern Fuegian thrust–fold belt after ~50 Ma (Maffione et al., 2010), while contrasting magnitudes and signs of post-60 Ma rotation (from 26° CCW to 26° clockwise —CW—) had been obtained from western Tierra del Fuego and Brunswick Peninsula, at the zone were structural trends change from NNW–SSE to NW–SE (Fig. 1). At least for the eastern thrust–fold belt, therefore, oroclinal bending (if occurred) should be older than the Paleogene.

Accordingly, in a recent tectonic model that integrates onshore geological studies with geophysical magnetic anomaly studies from the Scotia Arc, Torres Carbonell et al. (2014) support the interpretation of CCW rotation of the western margin of the Rocas Verdes Basin (Burns et al., 1980; Kraemer, 2003), simultaneously with its Late Cretaceous closure. This may have led to the creation of an incipient orogenic wedge that continued to rotate, acting as the Fuegian backstop that indented the foreland basin strata, in a similar manner than one of the analog models of Ghiglione and Cristallini (2007) has shown. However, the new model considers steady rotation from the Late Cretaceous to the early Paleogene (60 Ma) with the addition of the buttressing effect of the Río Chico Arch at the foreland side, which controlled the curvature of the advancing thrust front. After the initial rotation, the backstop moved northwards from 60 Ma to the early Neogene, further compressing the foreland basin against the Río Chico Arch and enhancing the curvature of the thrust–fold belt (Fig. 3).

This new model explains the pattern of thrust-front migration, and is consistent with the lack of significant rotations in post-50 Ma rocks at the apex of the curve in the Fuegian thrust–fold belt (Maffione et al., 2010; Poblete et al., 2014). According to this model the Fuegian limb of the Patagonian curve may consist of an outer (southern) orocline belt that rotated CCW, and an inner (northern) curved thrust belt whose curvature is attained due to interaction with an obstacle or promontory (the Río Chico Arch) (Fig. 3). The interpretation of the buttressing effect exerted by the craton margin promontory is supported by: a) the significant shortening increase in the frontal part of the curve from western Tierra del Fuego toward the apex of the Península Mitre Recess (Fig. 1); b) the coincidence of this apex with the southernmost edge of the Río Chico Arch (Fig. 1); c) the localization of frontal thrusts above steps in the Río Chico Arch topography (Fig. 2B-C) (Torres Carbonell et al., 2013a); and d) the convergence of shortening directions toward the promontory (Fig. 1).

2.2. Paleostress and shortening orientations in the Fuegian limb

Fault slip analyses from the western part of the Península Mitre Recess indicate a SW–NE maximum horizontal shortening direction for that portion of the thrust–fold belt, with a rotation to N–S directions in the easternmost measurements sites, at the apex of the recess (Diraison et al., 2000), where structural trends are E–W (Fig. 1) (Torres Carbonell et al., 2008b). A major problem with these data is that all faults measured are assumed to correspond to a single deformation phase, which is not consistent with the tectonic history of the Fuegian Andes (addressed above). Despite this problem, the data consistently indicate a shortening direction which is near-perpendicular to the structural trends for each site. At a more regional scale, Diraison et al. (2000) calculated a regional shortening axis oriented between N52° and N43° (i.e. SW–NE) for the Fuegian Andes.

On the other hand, the youngest tectonic disjunctive foliations in the internal thrust–fold belt (Late Cretaceous–Paleocene), which were formed by pressure-solution, progressively change orientation along a concave-to-the-north curve, matching the shape of the incipient Península Mitre Recess. This feature indicates a changing shortening direction along the curve, trending NE at the west and NW at the east (Fig. 1), interpreted as the result of a N–S oriented regional compression coupled with buttressing against the Río Chico Arch (Torres Carbonell et al., 2013b). In a similar manner, the Paleogene–early Neogene evolution of the thrust–fold belt and further development of the Península Mitre Recess do not fit a SW–NE regional shortening, neither a coaxial principal compression, which are not compatible with the formation of SW–NE trending folds and thrusts in the eastern flank of the recess. A N–S oriented regional compression combined with increasing buttressing against the Río Chico Arch better explain the pattern of thrust-front migration with convergence of the horizontal shortening trajectories toward the promontory (Torres Carbonell et al., 2013b, 2014).

3. Analogue modeling

Analogue modeling is a simplification of Nature; using this methodology, structures formed due to the deformation of rocks, whose in situ properties may be poorly known, can be modeled and investigated. The analog models addressed here are intended to qualitatively evaluate the structural evolution of the Fuegian thrust–fold belt according to: 1) the hypothesis of CCW rotation of the backstop simultaneous with the Late Cretaceous–early Neogene thrust–fold belt evolution (cf. Kraemer, 2003), and the hypothesis of Late Cretaceous–Paleocene rotation of the backstop followed by its northward movement proposed by Torres Carbonell et al. (2014) (Fig. 3); 2) the possibility of a prior curved backstop with different directions of indentation (e.g. northeastward according to Ghiglione and Cristallini, 2007; or northward); and 3) the possibility of a rectilinear backstop moving northeastward without rotation. All these hypotheses are evaluated with the additional influence of the Río Chico Arc as a rigid obstacle in front of the advancing thrust wedge.

Our main scope is not to obtain an exact reproduction of the orogenic curve, but to gain first-order insights into the influence of backstop rotations and a rigid foreland obstacle on its structural evolution. For this purpose, we performed five sandbox analogue experiments (Fig. 4). The geometry of the final sand wedge, the rotations and strains involved in its evolution, and the type of structures resulting from each simulation were then contrasted with the observed structural geometries and shortening magnitudes and directions in the Fuegian thrust–fold belt.

3.1. Experimental method

The model material was well-sorted and well-rounded dry quartz sand grains smaller than 600 μm. To a first approximation, such materials fail according to a linear Mohr envelope (Krantz, 1991). Their mechanical properties were measured with a modified Hubbert-type shear apparatus (Hubbert, 1951), which enables the determination of the ratio of normal-to-shear stress at failure. The coefficient of friction and the cohesion were then determined, indicating that the quartz sand has a friction angle of ~32.7°, similar to the values obtained

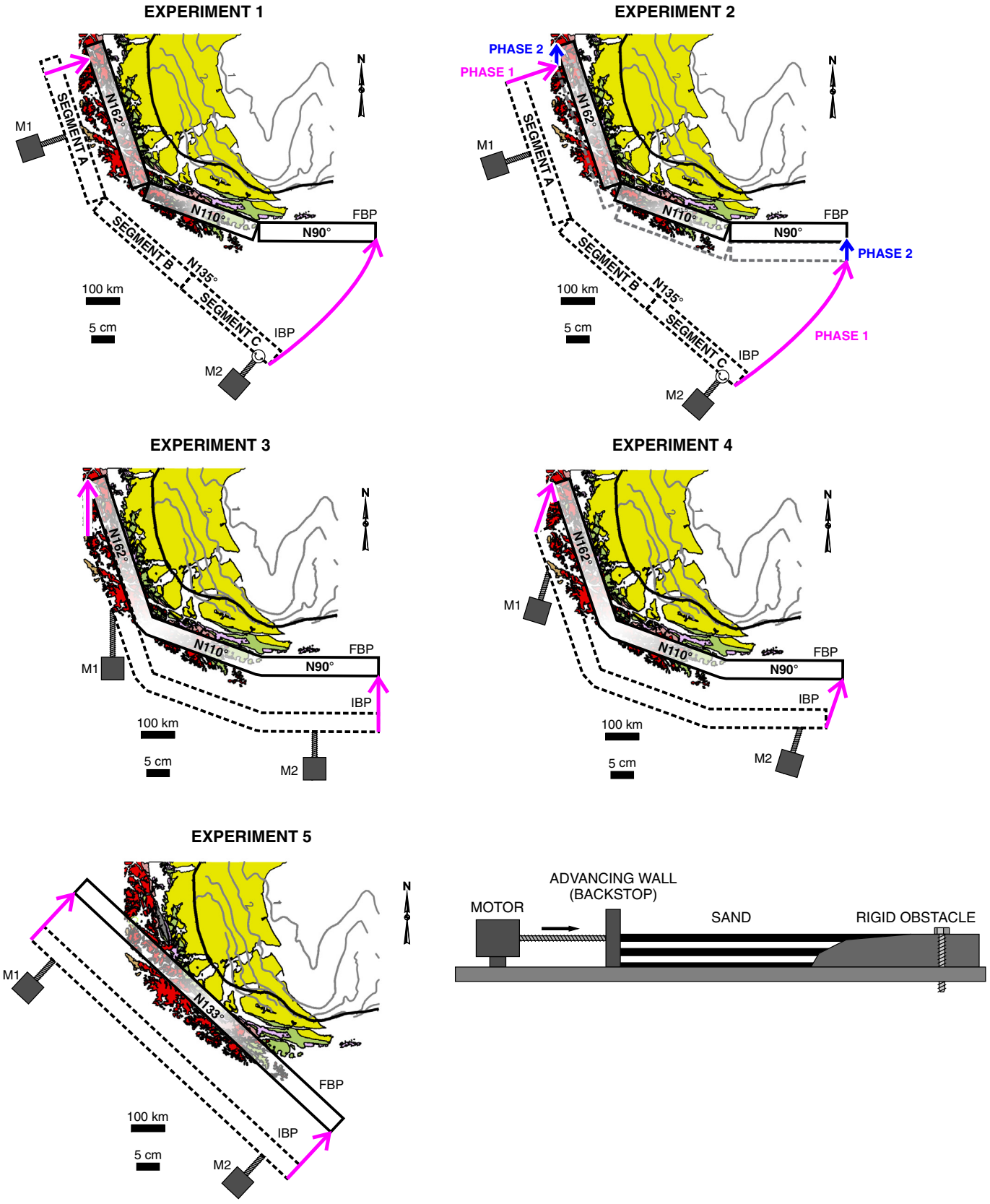

Fig. 4. Setup of the five experiments done. Each diagram shows the initial and final backstop position (IBP–FBP) of the models, and their location with reference to the Río Chico Arch (grey contours, see Fig. 1). The main geologic features of the natural prototype are also displayed for reference, with the southern block of the Fagnano Transform System in its restored position (see Figs. 1 and 3). The position of motors (M) is indicated as reference for Table 1. Magenta arrows correspond to backstops' movement paths (with blue arrows for the second phase of experiment 2). The diagram at the bottom right indicates the experimental setup in cross-section. (For interpretation of the references to color in this figure legend, the reader is referred to the web version of this article.)

experimentally for competent upper crustal rocks (Byerlee, 1978). Although the determination of cohesion is not very accurate with this method, this parameter was very low (<100 Pa) when compared with normal stress acting in the sandbox experiments (>1000 Pa). The basal friction (μb) between the quartz sand and the plastic sheet of the basal interface is low (μb = 0.16 ± 0.02), in agreement with an effective décollement in the upper crust, which in our simplified scenario represents the main detachment of the Fuegian thrust–fold belt (stair-stepping from Lower Cretaceous to Paleocene horizons, cf. Torres Carbonell et al., 2011; Zanella et al., 2014). This modeling strategy has been widely used by different authors (e.g., Davis et al., 1983; Konstantinovskaya and Malavieille, 2011). Thus these materials are good analogues for simulating brittle deformation in the uppermost crust (Hubbert, 1937, 1951; Sanford, 1959) assuming time independent rheological behavior, being suitable with our main objective of studying upper-crust deformation in the Fuegian thrust–fold belt.

The models described in this paper are roughly scaled such that 1 cm in the model simulates approximately 10 km in nature, and the vertical scale was exaggerated in order to better observe the generated structures in cross section. This strategy is suitable for the pursued objective of gaining first-order insights on the structural evolution of the Fuegian thrust–fold belt (see section 3.2). All the five models carried out contained alternating layers of sieved light and dark quartz sand, between 0.3–0.9 cm thick. The undeformed multilayers had an area of ~4550 cm^2 and a thickness of 3.5 cm.

In different experiments, the advancing wall (backstop) configuration was varied by changing its geometry, using articulated or fixed segments depending on the model purpose (Fig. 4). The moveable wall was connected to two computer-controlled step motors that pushed the wall segments in the desired direction. The rate of the displacements varied between experiments depending on the position of the motors and the chosen movements, as shown in Table 1 and Fig. 4. The arm pressed the sand against a rigid obstacle which simulated the basement promontory of the Río Chico Arch. This obstacle was constructed with an easily-molded rigid phenolic resin, in which the shape of the basement was copied at scale, based on the structural contours published by Biddle et al. (1986) and Yrigoyen (1989).

In all the experiments a total of ~12 cm of displacement was applied to the part of the arm that represents the western backstop of the curve, or to the whole arm when it acted as a non-articulated backstop (experiments 3 to 5). In experiments where the arm was articulated, the maximum displacements reached 35 cm (Table 1). In our simplified scheme, these magnitudes were selected to obtain a conveniently sized sand wedge that allows focusing on the effects of backstop movement and rigid obstacle geometry, and they are reasonable in the context of the highly variable shortening estimations along the Patagonian curve (Fig. 1) (Fosdick et al., 2011; Ghiglione et al., 2009; Torres Carbonell and Dimieri, 2013).

Except for the fifth experiment, the final position reached by the backstop was referenced to the early Neogene location of the backbone of the Fuegian Andes with respect to the fixed foreland basement prior to 50 km left-lateral offset along the Fagnano transform system (Fig. 4) (Torres Carbonell et al., 2008a). The top surfaces of each experiment were recorded every minute using zenithal digital photography, and scanned with a laser at regular time intervals to obtain their topography. The deformed models were solidified using gelatin, serially sectioned roughly perpendicular to the mobile wall, and photographed. The surface DEM obtained from the laser scanner and the serial cross-section photographs were integrated in a 3D view in Move software (version 2014.2, Midland Valley) in order to determine the 3D structure of the sand wedge. This was performed by mapping faults and horizons in each cross-section, and further construction of fault and horizon surfaces in 3D.

The digital photographs taken every minute were processed using optical image correlation techniques (PIV: particle imaging velocimetry). We used the MatPIV v. 1.6.1 software (Sveen, 2004) that allows quantifying high-resolution displacement fields between two successive images within the grain-size range, without the restriction of limited marker points (Adam et al., 2005; White et al., 2001; Wolf et al., 2003).

PIV results were reprocessed with the GEODEF 1.1 software (Yagupsky, 2010), obtaining the incremental and accumulative surface strain patterns. This process considers the directional derivatives for each incremental vector between two pictures (1 min span), thus allowing the calculation of the incremental strain matrix for each point of the model. The spatial and temporal pattern of strain accumulation were thus obtained (cf. Adam et al., 2005), providing a quantification of all deformation components in the experiments.

Table 1
Velocity (V) and displacement (S) of motors used in the experiments. See position of motors for each experiment in Fig. 4.

	Motor 1		Motor 2	
	V (cm/h)	S (cm)	V (cm/h)	S (cm)
Experiment 1	13.8	11.8	41.1	35
Experiment 2				
Phase 1	13.8	12.5	38.9	35
Phase 2	12.6	4	12.6	4
Experiment 3	13.8	12.5	13.8	12.5
Experiment 4	13.8	12.5	13.8	12.5
Experiment 5	13.8	12.5	13.8	12.5

3.2. Experimental simplifications and limitations

The geometries and rheologies of analogue experiments necessarily simplify the complexity of the natural prototype. There are two main simplifications in the setup of our models, which result from the use of analog experiments aiming to achieve a qualitative evaluation of the Fuegian thrust–fold belt structural evolution. At first, the length scale ratio was selected in such a way that 1 cm represents a length of about 10 km in nature, but with considerable vertical exaggeration in order to gain a better resolution of fault patterns in cross-section. This prevents a quantitative comparison between experiments and natural structures, but without hampering our main objective of analyzing fault shapes and kinematics, and comparing shortening variations along strike, instead of their absolute magnitudes.

Secondly, the strength of the rigid phenolic resin used to mimic the Río Chico Arch is some orders of magnitude higher than sand, so this material behaved as a rigid, undeformable basement block. This approximation has been widely used in analogue modeling (e.g. Bonini et al., 1999, 2000; Koyi and Maillot, 2007), and also applied, as we did, to describe the effect of foreland obstacles on the development of curved orogens (Macedo and Marshak, 1999; Lickorish et al., 2002; Gomes et al., 2003). Furthermore, we consider it as a valid analog for the frontal part of the Fuegian thrust–fold belt, where the contractional structures affecting the sedimentary cover do not affect the Río Chico Arch basement, and in some cases the frontal faults even ramp-upwards in front of pronounced basement scarps (Fig. 2B-C) (Torres Carbonell et al., 2013a). This style of deformation was successfully reproduced in our experiments (section 4).

Finally, the experimental setup in our models does not account for plate flexure and isostatic compensation beneath the growing wedges, for the role of pore fluid pressure and for temperature variations. These limitations are very common in sandbox experiments and have been shown not to significantly affect the first-order model results (e.g. Malavieille, 1984; Liu et al., 1992; Koyi, 1995; Gutscher et al., 1996; Storti et al., 2000).

3.3. Models' deformation

3.3.1. Experiment 1

Experiment 1 was intended to test the behavior of the sand wedge under compression by a rotating, articulated indenter (Fig. 4). The

model resembles the theoretical behavior of the Fuegian thrust–fold belt being compressed by rotation of the Fuegian backstop during its whole contractional history (Late Cretaceous–early Neogene). The backstop was segmented in three parts (A, B and C) and started with a curved shape, with segment A striking N162° (as seen in Fig. 4, in all the experiments the direction of North is calibrated by the present-day position of the undeformable parts of the model), and segments B and C both parallel with a strike of N135° (Fig. 4). During the first 42 min segments B and C were fixed to each other and rotated 25° CCW with respect to segment A, which was simultaneously pushed towards the NE (N72°) 11.8 cm. The next 9 min segments A and B were attached in order to form a fixed curve where A strikes N162° and B N110°, and both move toward N72°. Segment C was unfixed from B; this resulted in the further CCW rotation of additional 20° of the C segment, which attained a final N90° strike.

3.3.2. Experiment 2

In this experiment, we tested the theoretical behavior of the Fuegian thrust–fold belt being compressed by rotation of the Fuegian backstop only during the first part of its evolution, and with a northward push of the non-rotating backstop during the final stage of its contractional history (Fig. 4). The backstop evolution was thus modeled in two phases. The first phase is similar to experiment 1: the segmented curved backstop rotates to attain a shape with the same orientation than the previous experiment (segment A: N162, B: N110°, C: N90°). The path of segment rotations and movements during this phase is the same as in experiment 1. The difference stands in the final position of the curved backstop, which in this case is 4 cm south of that acquired in the first experiment. The second phase of experiment 2, then, involves 4 cm of northward movement of the curved backstop, without rotations, until the final position is attained (Fig. 4).

3.3.3. Experiment 3

In the third experiment, we modeled the behavior of the Fuegian thrust–fold belt subjected to a straight northward push from an originally curved backstop, without rotation. The backstop starts with the same final shape than the previous experiments (segment A: N162, B: N110°, C: N90°) and is pushed 12.5 cm northward (Fig. 4).

3.3.4. Experiment 4

In experiment 4 we tested the behavior of the Fuegian thrust–fold belt when the curved backstop pushed toward N20°, i.e. resembling a SSW–NNE compression. The experiment was similar to experiment 3, but differed in the direction of backstop movement (Fig. 4).

3.3.5. Experiment 5

In experiment 5 we tested the behavior of the Fuegian thrust–fold belt subjected to the push of a straight backstop oriented N133°, and pushing toward N43°, in accordance with the shortening axis calculated by Diraison et al. (2000). The backstop would be analogous to the initial Fuegian Andes orogenic wedge moving northeastward without rotation, pushed by subduction at its Pacific side. The distance pushed in this case was also of 12.5 cm (Fig. 4).

4. Results

4.1. Experiments 1 and 2

The first two experiments reveal very similar results, thus are here analyzed together. The curved geometry of the sand wedge was attained from the beginning of deformation due to the synchronous formation of a curved backstop (Figs. 5A and 6A). On the other hand, the rigid obstacle exerted a buttressing effect, since it restrained the advance of the thrust front enhancing the recess in the sand wedge (Figs. 5B and 6B).

The middle and eastern segments of the sand wedge clearly rotated CCW accompanying the rotation of the backstop. Rotations in the western limb, on the other hand, are of significantly less magnitude and CW. Indeed, they are constrained to the active fault traces (few millimeters wide) (Figs. 5C and 6C), and are related to non-coaxial strain in the fault zones. In the second stage of experiment 2, this CW rotation in fault traces of the western limb was slightly enhanced.

At the end of the experiments, the branch line of the frontal thrust was located at the edge of the rigid obstacle, and the frontal thrust surface molded the obstacle's form, evidencing buttressing (Figs. 5B, D–G and 6B, D–G). The dilatation obtained from the incremental strain analysis shows this very clearly, revealing that the frontal faults were nucleated tracing the structural contours of the rigid obstacle (Fig. 7A–B). This buttressing also caused a difference between the initial and final curve's shapes. The former was almost parallel to the backstop, while the latter mimicked the rigid obstacle shape (Figs. 5A–B and 6A–B).

Quantitative shortenings along the curved sand wedges are difficult to measure accurately. Shortening estimations from map-view or cross-sections are problematic to assess since, except for the segments of the curve which moved in a direction orthogonal to the backstop and without rotation, no plane-strain can be assumed for any other cross-section plane. However, it is possible to qualitatively compare shortenings from the map-view when we take into consideration the strain ellipses and dilatation obtained from the PIV reprocessing (see Section 3.1).

This analysis reveals that in experiments 1 and 2 the larger trajectory of the southern segment of the rotating backstop, which moved faster, increased the contraction at the eastern segment of the curve. The buttressing effect of the rigid element also enhanced the contraction at the apex of the curve. However, when the easternmost segment of the backstop rotated freely, no significant contraction occurred at the apex, while the limbs shortened further. In experiment 2, however, the apex accumulated more contraction than the limbs during the second phase (N-directed push), mainly in the frontal fault normal to the transport direction. The buttressing effect is clearly observed in cross-sections, as illustrated by the development of more complex structures at the apex because of the higher shortening (Figs. 5E–G and 6E–G).

Slip vectors in experiments 1 and 2 were perpendicular or highly oblique to the active faults, and tended to converge towards the rigid obstacle (Figs. 5C and 6C). Deformation ellipses also showed contraction normal to the structural trends, and extension parallel to them. However, during the last stages of the experiments, in the zone where the curvature of the sand wedge was higher, deformation ellipses were rotated and they showed contraction parallel to the orogenic front (Figs. 5A–B and 6A–B). The same effect was observed in ellipses related to out-of-sequence thrusts perpendicular to the backstop near the hinge zones (Fig. 5B).

In the final part of experiment 2, which involved a northward push of the backstop, the slip vectors continued to be perpendicular or highly oblique to faults in the axis of the curve and eastern limb. On the other hand, in the western margin of the curve the vectors were less oblique, and a right-lateral component of fault slip was manifest (Fig. 6C). However, at the end of the experiment slip vectors tended to attain more perpendicular orientations with the frontal fault, especially after interaction with the rigid obstacle became more intense.

4.2. Experiment 3

The curvature of the sand wedge was attained from the beginning of experiment 3, reflecting the influence of the prior curved backstop on its formation. With continued advance of the backstop and sand wedge, the buttressing against the rigid obstacle enhanced the recess (Fig. 8A–B).

CW rotation was observed in the western limb constrained to the traces of right-lateral oblique faults (see below), due to rotation within the narrow fault zones. Conversely, in the eastern limb minor CCW rotations were observed only when the frontal fault reached the position of

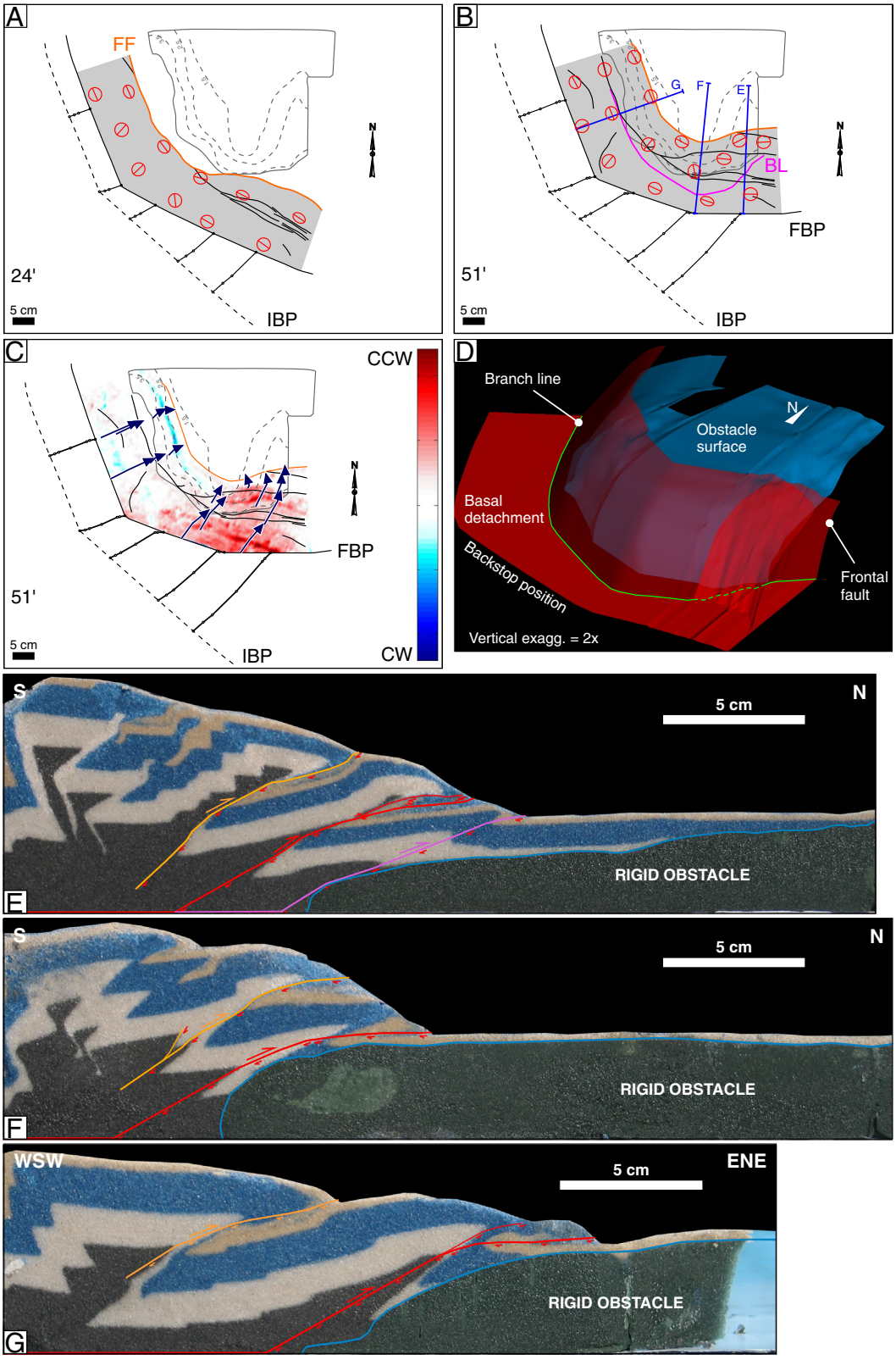

Fig. 5. Summary of results of experiment 1. A–B. Diagram of the experiment at 24 and 51 min (end of experiment) showing: initial and final backstop positions (IBP–FBP), location of the rigid backstop with structural contours (grey lines), surface traces of faults (black lines) in the sand wedge (gray shading), position of the frontal fault (FF) and its branch line (BL), accumulated strain ellipses from PIV reprocessing, and position of cross-sections in E–G. C. Areas of the final sand wedge with accumulated rotations and flow lines from PIV reprocessing. D. 3D view of the final wedge showing the geometry of the frontal fault and rigid obstacle. E–G. Selected cross-sections (located in B) of the final sand wedge, with interpreted faults. Curved fault segments are portions affected by backthrusting.

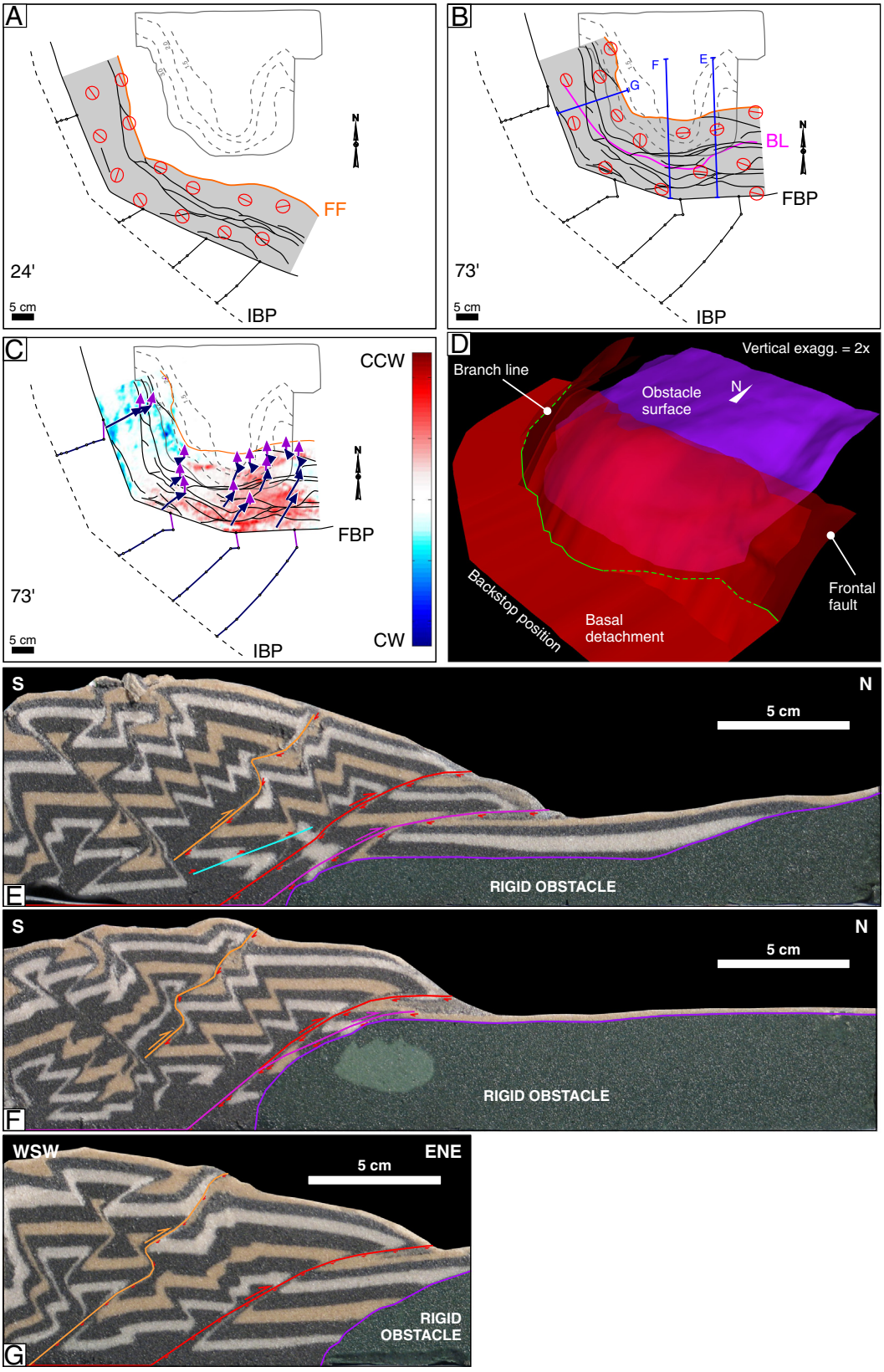

Fig. 6. Summary of results of experiment 2. A–B. Diagram of the experiment at 24 and 73 min (end of experiment) showing: initial and final backstop positions (IBP–FBP), location of the rigid backstop with structural contours (grey lines), surface traces of faults (black lines) in the sand wedge (gray shading), position of the frontal fault (FF) and its branch line (BL), accumulated strain ellipses from PIV reprocessing, and position of cross-sections in E–G. C. Areas of the final sand wedge with accumulated rotations and flow lines (phase 1 in blue, phase 2 in purple) from PIV reprocessing. D. 3D view of the final wedge showing the geometry of the frontal fault and rigid obstacle. E–G. Selected cross-sections (located in B) of the final sand wedge, with interpreted faults. Curved fault segments are portions affected by backthrusting.

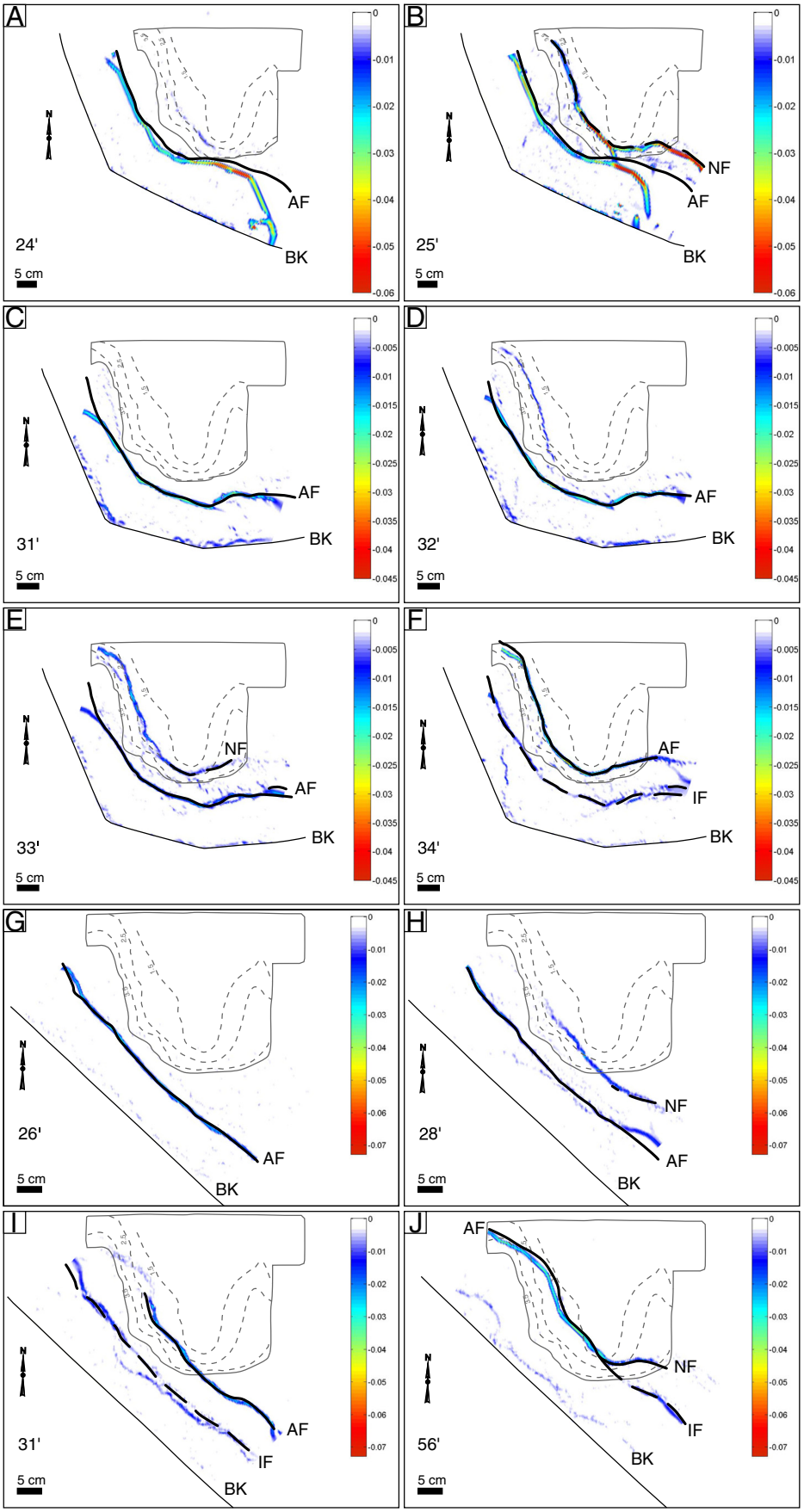

Fig. 7. Dilatation from PIV reprocessing for different stages of experiments 1 (A–B), 4 (C–F) and 5 (G–J). BK: backstop, AF: main active fault, NF: new fault being formed, IF: fault becoming inactive.

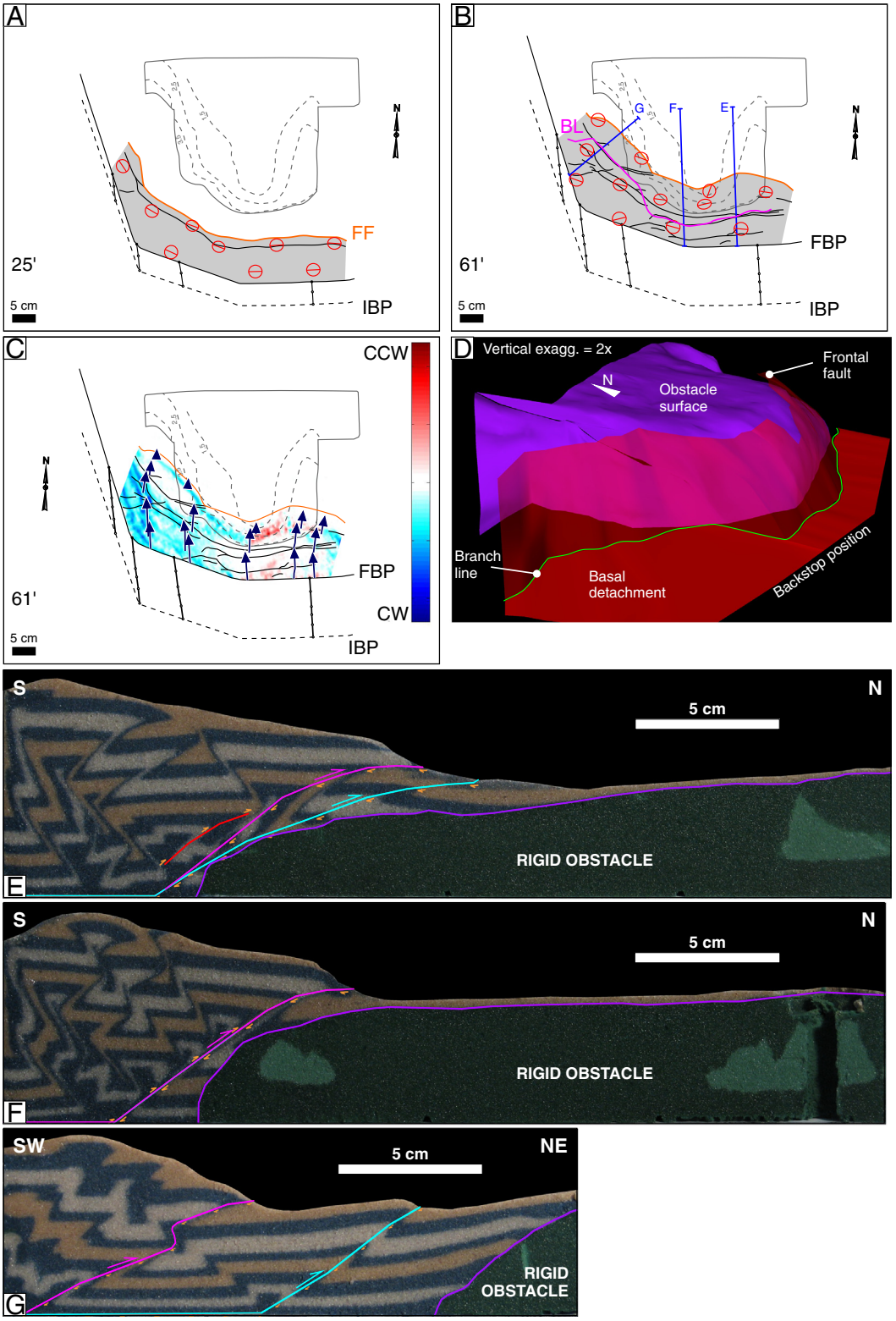

Fig. 8. Summary of results of experiment 3. A–B. Diagram of the experiment at 25 and 61 min (end of experiment) showing: initial and final backstop positions (IBP–FBP), location of the rigid backstop with structural contours (grey lines), surface traces of faults (black lines) in the sand wedge (gray shading), position of the frontal fault (FF) and its branch line (BL), accumulated strain ellipses from PIV reprocessing, and position of cross-sections in E–G. C. Areas of the final sand wedge with accumulated rotations and flow lines from PIV reprocessing. D. 3D view of the final wedge showing the geometry of the frontal fault and rigid obstacle. E–G. Selected cross-sections (located in B) of the final sand wedge, with interpreted faults. Curved fault segments are portions affected by backthrusting.

the rigid obstacle. This fault traced the shape of the rigid obstacle, thus some left-lateral oblique-slip caused the observed rotation in the fault zone (Fig. 8C). The final curvature of the frontal fault molded the rigid obstacle form, and had a different shape than the one attained at the beginning of the experiment, which was parallel to the backstop (Figs. 8A, B and D).

The PIV reprocessing shows that any fault which was not perpendicular to the movement direction of the backstop (northward) has accommodated oblique slips, therefore it is not convenient to compare shortenings in cross-section for the reason discussed above. However the contractional component of strain was clearly higher at the apex of the curve (Fig. 8B), especially when the sand wedge started to collide with the rigid obstacle, and was even higher in the faults that were orthogonal to the slip vectors. Cross-sections also reveal the buttressing effect on the development of structures, which are more complex at the apex of the curve (Fig. 8E–G).

The slip vectors during experiment 3 were perpendicular or highly oblique to faults in the axis of the curve and eastern limb, but less oblique in the western limb, which revealed right-lateral oblique faulting (Fig. 8C). However, as deformation continued many out-of-sequence thrusts formed perpendicular to N–S slip vectors relieving part of that limb's oblique-slip faulting (Fig. 8B).

Strain ellipses also showed contractional deformation in the eastern limb and axis of the curve, with long axes parallel to the structural trends; whereas the long axes were oblique to the faults in the western limb (Fig. 8A–B). Long axes perpendicular to the structural trend were also observed in the most curved part of the sand wedge.

4.3. Experiment 4

During the beginning of experiment 4 the sand wedge attained an initial curvature, parallel to the backstop shape. This curve was afterwards enhanced during increased interaction between the sand wedge and the rigid obstacle (Fig. 9A–B).

CW rotations in the western limb of the curve and CCW in the eastern limb were observed constrained to the mm-wide fault zones, which showed a right-lateral or left-lateral component of oblique-slip, respectively (see below). In the eastern limb, however, this fault zone rotation was not observed until the frontal fault started to interact with the rigid obstacle. At the end of the experiment, a well-defined NE–SW axis of symmetry separated fault traces from both limbs, with opposite rotation signs. A lack of rotation in the apex was also very evident (Fig. 9C).

The dilatation obtained from the incremental strain analysis reveals that the frontal faults nucleated along the structural contours of the rigid obstacle and the deformation was progressively transferred from the fault that was being abandoned to the newly formed (Fig. 7C-F). The final shape of the frontal fault, therefore, was similar to the shape of the rigid obstacle (Fig. 9D).

The PIV reprocessing shows a higher contraction at the apex of the curve after collision between the sand wedge and the rigid obstacle, especially in the western part of the apex where slip was normal to fault traces. Displacement trajectories show that faults normal to the backstop's movement direction (northeastward), especially those located in the axis of the curve, were mostly thrusts. Right-lateral oblique-slip was apparent in the western limb, although late out-of-sequence faults and backthrusts normal to the backstop movement direction accommodated the deformation in that portion of the curve during the final part of the experiment. In the eastern limb some minor left-lateral oblique faults were formed (Fig. 9C). Long axes of strain ellipses were mostly parallel or slightly oblique to the deformation front (Fig. 9A-B), although shortening parallel to the frontal fault trace was observed in the most curved portion of the sand wedge. In cross-section, the deformation is more complex around the apex of the curve, were opposition to fault propagation was more intense (Fig. 9E–G).

4.4. Experiment 5

In experiment 5, the curvature was not acquired until the sand wedge started to interact with the rigid obstacle, which restrained the thrust front advance creating the recess (Fig. 10A-B). Likewise, rotations in the mm-wide fault zones were observed since the moment when the sand wedge collided with the rigid obstacle. A central region of slow propagation and without rotation divided the NW limb, with slight fault zone CW rotations, from the SE segment with faults showing minor CCW rotations. Only in the last stage where an oblique left-lateral fault forms in the SE segment, a stronger CCW rotation is observed in the fault zone (Fig. 10C). The 3D reconstruction and the dilatation from PIV reprocessing show that the fault front location was conditioned by the shape of the rigid obstacle (Figs. 7G–J and 10D).

The net amount of shortening in any cross-section normal to the backstop was the same (12.5 cm) (Table 1), but the percentage of shortening increased towards the western part of the curve, where the width of the sand wedge was shorter (Fig. 10E–H). Accordingly, strain ellipses reveal higher contraction in the western part, where buttressing against the obstacle occurred, while it decreased toward the south and SE, beyond the southern border of the obstacle where no buttressing occurred (Fig. 10A–B). The buttressing effect caused the higher complexity of structures in cross-sections in the part of the sand wedge with more interaction with the rigid obstacle, around the curve's apex (Fig. 10E–H).

Both slip vectors and strain ellipses in this experiment indicated mostly pure thrust motion perpendicular to the backstop movement direction (northeastward) (Fig. 10C). Only during the last stage of deformation, when a curved ramp developed in the southern part of the sand wedge, vectors revealed a component of left-lateral oblique-slip in that region.

4.5. Summary of results

It is clear from the results of experiments 1 to 4 that the prior existence or synchronous formation of a curved backstop determined the initial curved shape of the deformed wedge, a result previously obtained in similar experiments (Ghiglione and Cristallini, 2007). In experiment 5, in which the backstop is rectilinear, the curve forms only after the sand wedge and the rigid obstacle collide (Fig. 10A–B). In the rest of the experiments the initial curve is enhanced during collision, with a final shape conditioned by the rigid obstacle's geometry (Figs. 5–9). This geometry clearly defines the location of the frontal faults, which nucleate along the obstacle's structural contours (Fig. 7), and respond, as mentioned in section 3.2, to the imposed strength contrast between sand and the rigid obstacle's material.

In experiments 1 and 2, with a rotational backstop, the middle and eastern segments of the sand wedge clearly accompanied the CCW backstop rotation. The western limb, however, did not rotate as a whole. CW rotations were limited to the mm-wide fault zones and depended on the obliquity of the fault slip vector, and were more notable when the sand wedge interacted the most with the rigid obstacle. The same fault zone rotations are observed in the rest of the experiments, where none of the wedge segments rotated as a whole. Both the sign and magnitude of rotations were dependent on the orientation of the faults with respect to the slip vectors. Thus, right-lateral oblique faults in the western limb of the wedge rotated CW, and left-lateral oblique faults in the eastern limb rotated CCW. No significant rotations were accumulated in the apex (Figs. 8C and 9C). The fact that fault zone rotations were enhanced since the moment of collision with the rigid obstacle highlights the role of buttressing as a cause of contrasting rotations in both limbs of the curve. This behavior is even more notorious in experiment 5, in which fault-zone rotations only started when the sand wedge collided with the rigid obstacle.

The buttressing against the rigid obstacle clearly influenced the zones where the contraction was higher, especially at the apex of the curve, as revealed by the PIV reprocessing and in the cross-sections from all the experiments. This buttressing also strongly defines the deformation style: where the impediment to fault propagation was higher, more backthrusts and out-of-sequence thrusts developed.

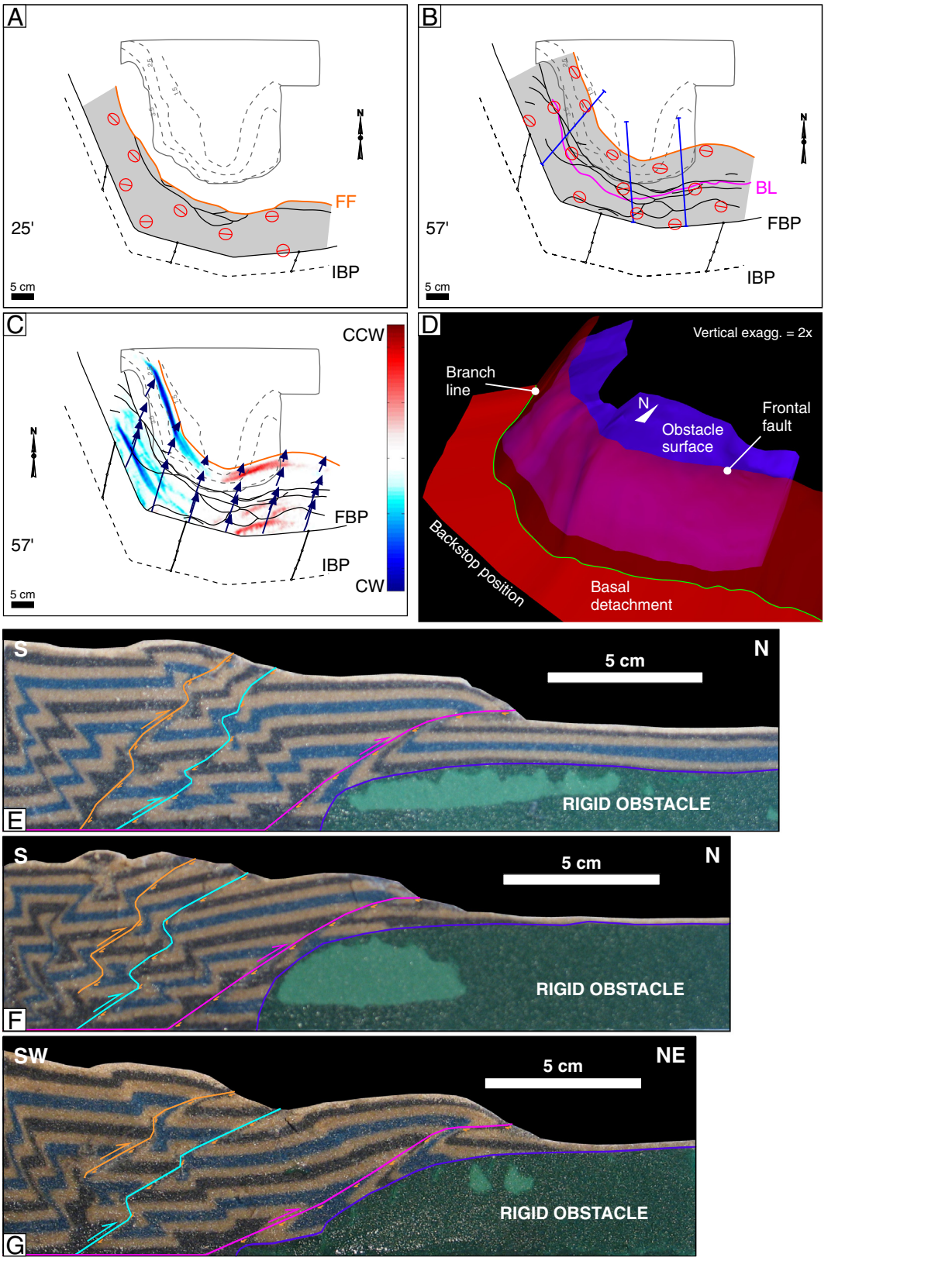

Fig. 9. Summary of results of experiment 4. A–B. Diagram of the experiment at 25 and 57 min (end of experiment) showing: initial and final backstop positions (IBP–FBP), location of the rigid backstop with structural contours (grey lines), surface traces of faults (black lines) in the sand wedge (gray shading), position of the frontal fault (FF) and its branch line (BL), accumulated strain ellipses from PIV reprocessing, and position of cross-sections in E–G. C. Areas of the final sand wedge with accumulated rotations and flow lines from PIV reprocessing. D. 3D view of the final wedge showing the geometry of the frontal fault and rigid obstacle. E–G. Selected cross-sections (located in B) of the final sand wedge, with interpreted faults. Curved fault segments are portions affected by backthrusting.

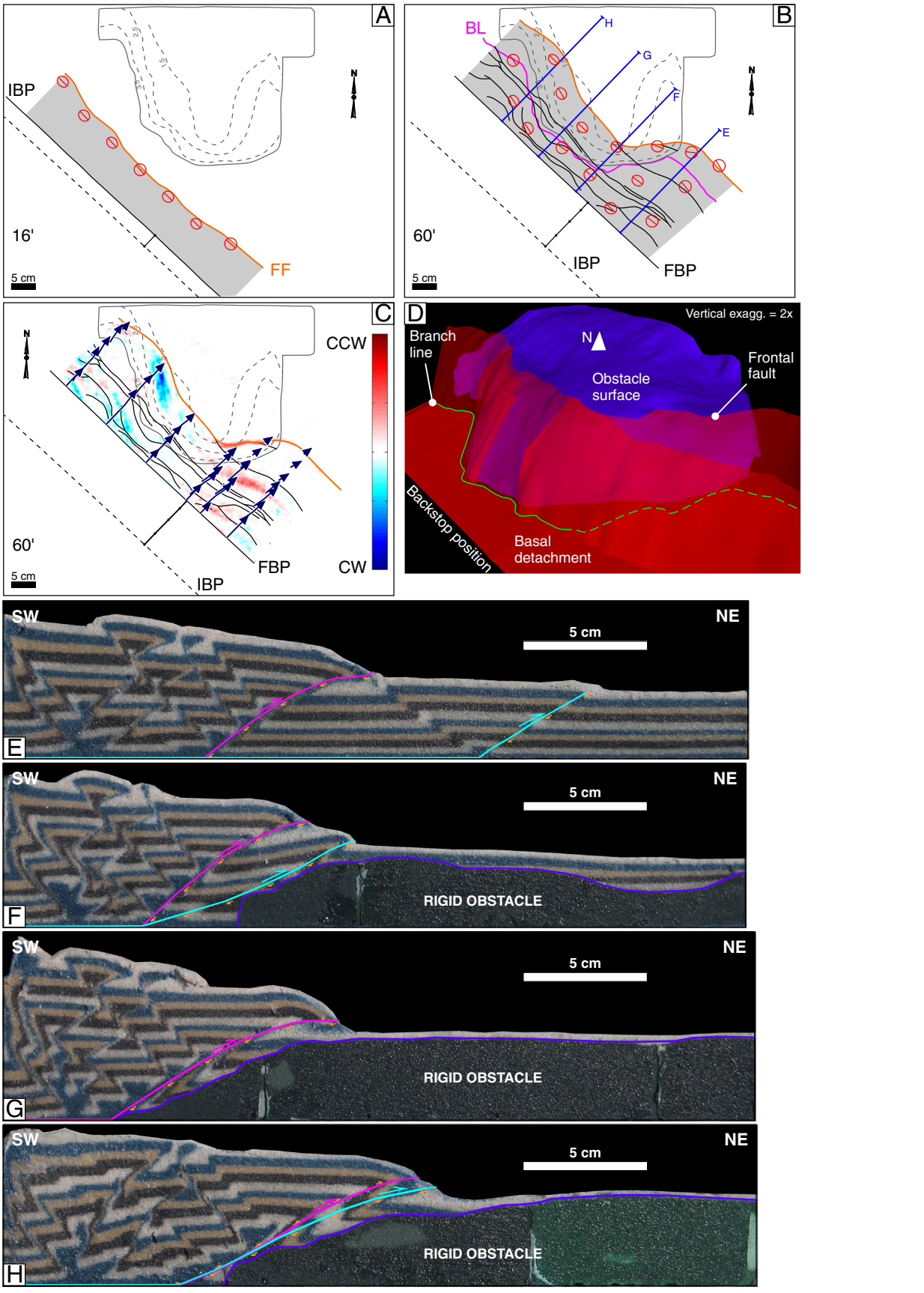

Fig. 10. Summary of results of experiment 5. A–B. Diagram of the experiment at 16 and 60 min (end of experiment) showing: initial and final backstop positions (IBP–FBP), location of the rigid backstop with structural contours (grey lines), surface traces of faults (black lines) in the sand wedge (gray shading), position of the frontal fault (FF) and its branch line (BL), accumulated strain ellipses from PIV reprocessing, and position of cross-sections in E–H. C. Areas of the final sand wedge with accumulated rotations and flow lines from PIV reprocessing. D. 3D view of the final wedge showing the geometry of the frontal faults and rigid obstacle. E–H. Selected cross-sections (located in B) of the final sand wedge, with interpreted faults. Curved fault segments are portions affected by backthrusting.

Mainly thrust faulting was observed in experiments 1 and 2, where slip trajectories converged toward the rigid obstacle and strain ellipses revealed contraction normal to the structural trends. It is notable, however, that some amount of orthogonal flexure in the rotating wedge appears to have caused contraction parallel to the orogenic front in the frontal part of the apex (Figs. 5B and 6B). This latter effect was also observed in experiments 3 and 4 (Figs. 8B and 9B).

In the final stage of experiment 2 and in experiment 3, which involved a northward push of the backstop, and in experiment 4 with a northeastward push, a right-lateral component of fault slip was manifest in the western limb. In that portion, faults behaved as sidewall or oblique ramps of the frontal thrust. However, in experiment 3, new out-of-sequence thrusts formed perpendicular to N–S slip vectors relieving the movement on the sidewall ramps (Fig. 8A-C). Similarly, in experiment 4, the initial right-lateral oblique faults in the western limb were in part relieved by some backthrusts and out-of-sequence thrusts as deformation continued (Fig. 9A-B).

5. Comparison with the Fuegian thrust–fold belt

5.1. Rotations

Recent results from paleomagnetic studies in Tierra del Fuego indicate that no significant rotations occurred since ~50 Ma in the Fuegian thrust–fold belt at the apex of the Península Mitre Recess (Maffione et al., 2010). Away from the Península Mitre Recess, in the area where the Patagonian curve develops a strike-change from NNW–SSE to NW–SE (Brunswick Peninsula and western shore of Tierra del Fuego), characteristic remanent magnetizations reveal either 26° CCW and 26° CW post-60 Ma rotations (Poblete et al., 2014). These authors are more confident on the 26° CCW rotation indicated by their data, and consider it is related to non-coaxial deformation during the Paleogene, or to a gradient of shortening magnitudes that increase toward the east.

In our models, experiments 1 and 2 are the only ones that show CCW rotations accompanying the backstop rotation, even in the middle part of the curve, although with little magnitude at the wedge front (Fig. 11). Least intense rotations are observed at the front in experiment 2, which involved a second phase of convergence without backstop rotation (Figs. 4 and 6C). This is consistent with the CCW rotations observed at Brunswick Peninsula (Poblete et al., 2014), which would be geographically equivalent to the backstop hinge between the western and middle segments (segments A and B in Fig. 4). It is also consistent with the lack of rotations reported by Maffione et al. (2010) at the frontal structures in the apex of the Península Mitre Recess.

Experiments 3 to 5, on the other hand, show no rotations of the sand wedge as a whole. The only rotations are constrained to the narrow (mm-wide) fault zones, and are a result of non-coaxial deformation within these zones (Fig. 11). Each new fault was born with a curved trace that molded the rigid obstacle geometry, thus configuring a primary arc (Marshak, 2004). This lack of rotations seems also coherent with the paleomagnetic results from the frontal structures of the thrust–fold belt obtained by Maffione et al. (2010) and Poblete et al. (2014).

5.2. Strains

Regarding strains, experiments 1 and 2 both show more complex structures and higher contraction at the apex of the curve (Fig. 11), which is a situation comparable with that described in nature. Accordingly, an increase in shortening from less than 5% to more than 20% has been reported toward the apex of the Península Mitre Recess in the thrust–fold belt front, as well as a more complex structural style compared to the style in the western limb of the recess (Fig. 11) (Alvarez-Marrón et al., 1993; Torres Carbonell et al., 2011, 2013a).

An important aspect of experiments 1 and 2 is that the long axes of strain ellipses changed from orogen-parallel during early stages to orthogonal during the last stages, at places where rotation of the curve was higher (Figs. 5B and 6B). This is in coincidence with examples of field structures, such as N–S trending folds, and some paleostress tensors from fault slip inversion, which indicate a late orogen-parallel contraction due to bending in the apex of the Península Mitre Recess (Fig. 2A) (Torres Carbonell et al., 2011; Maestro et al., 2015).

In addition, experiments 1 and 2 are the only ones that effectively show a convergence of slip vectors toward the obstacle along the complete thrust front (for experiment 2 more notably before the last phase of northward push) (Figs. 5C, 6C, and 11). This is consistent with NNW–SSE short axes of accumulated strain ellipses in the eastern limb (Figs. 5B, 6B, and 11), coinciding with the natural structures in the eastern limb of the Península Mitre Recess (Figs. 1 and 11). These structures include Late Cretaceous–Danian disjunctive foliations formed by pressure-solution and Late Cretaceous–Paleogene thrusts sheets and related folds, all oriented ENE–WSW (Torres Carbonell et al., 2011, 2013b).

Experiments 3 and 4 also show an increase in contractional strain toward the apex, and experiment 3 in particular reveals NNW–SSE shortening directions in the eastern limb. However, both experiments imply the development of oblique-slip faults with right-lateral component in the western limb, which in the experiment 4 develops simultaneously with a left-lateral oblique-slip system in the eastern limb (Fig. 11). In both experiments, and more notably in experiment 3, there is also development of backthrusts and out-of-sequence thrusts oriented E–W (perpendicular to slip vectors) in the western limb (Figs. 8 and 11). This kind of structures and fault styles are not consistent with the conspicuous N–S striking structures described for the western limb of the Patagonian curve (Fosdick et al., 2011; Ghiglione et al., 2009).

Experiment 5 is the one that differs most from the natural prototype. It shows an almost homogeneous NE–SW oriented shortening along the sand wedge, with development of NW–SE thrusts along the complete wedge, except locally at the front of the younger fault that mimics the southern border of the obstacle at the end of the experiment (Figs. 10 and 11). Also, shortening is higher at the western limb, where thrust advance was strongly restricted by the obstacle (Fig. 11). Thus, shortening magnitudes and directions, as well as orientation of structures in experiment 5 differ from those recognized in the apex and eastern part of the Península Mitre Recess.

5.3. Summary

The experiments in this work show that the use of a curved backstop that interacts with a rigid obstacle at the foreland results in structural features in the sand wedge that are similar to the ones observed in the curved Fuegian thrust–fold belt. The buttressing against the undeformable rigid obstacle was notably developed in all the experiments, and successfully reproduced the structural style of the frontal thrust–fold belt as reported by subsurface data (e.g. Fig. 2B-C) (Torres Carbonell et al., 2013a). However, only with a rotating backstop the slip vectors and the shortening directions are highly oblique to the fault trends along the complete curve, since curved backstops moving in a fixed direction produce regions of the curve with dominant oblique-slip or strike-slip faulting. Thus, experiments 1 and 2 with a rotational backstop better resemble the natural prototype (Fig. 11). These experiments imply a backstop rotation comparable to the inferred rotation of the southwestern margin of the Rocas Verdes Basin during its closure (e.g. Kraemer, 2003), and a deformed sand wedge comparable to the Upper Cretaceous–Cenozoic sedimentary cover of the Fuegian thrust–fold belt that was compressed against the Río Chico Arch during the backstop rotation (e.g. Torres Carbonell et al., 2013a, 2014).

Experiment 2 is attractive since it involves a final N-directed movement of the whole orogenic system (without further rotation), which enhances the shortening against the obstacle, and is comparable with tectonic reconstructions from magnetic anomalies in the Scotia

EXPERIMENT	ROTATION			STRAIN GRADIENT	SHORTENING DIRECTIONS	DOMINANT FAULT TYPE & SLIP DIRECTIONS
	WEST LIMB	APEX	EAST LIMB			
1	CW (LIMITED TO FAULT ZONES)	CCW	CCW	POSITIVE TOWARD APEX	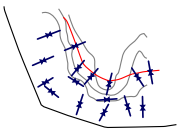	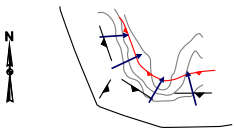
2	CW (LIMITED TO FAULT ZONES)	CCW	CCW	POSITIVE TOWARD APEX	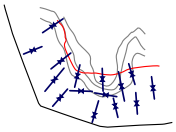	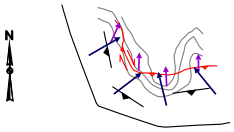
3	LIMITED TO FAULT ZONES CW	CW-CCW	CCW	POSITIVE TOWARD APEX	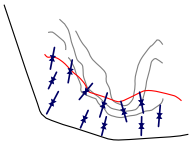	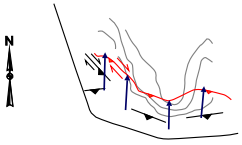
4	LIMITED TO FAULT ZONES CW	NO	CCW	POSITIVE TOWARD APEX	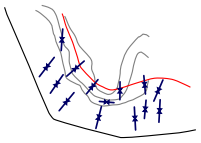	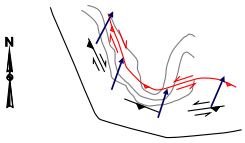
5	LIMITED TO FAULT ZONES CW	NO	CCW	POSITIVE TOWARD W LIMB	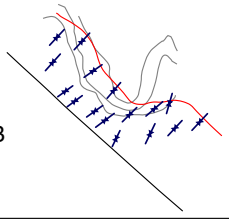	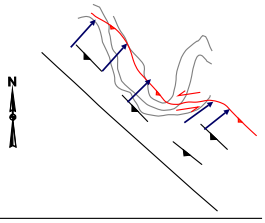
NATURAL PROTOTYPE	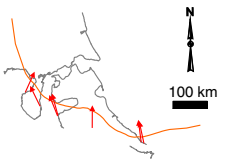			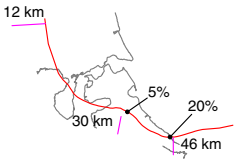	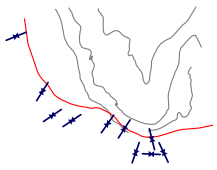	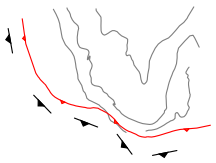

Fig. 11. Comparison of results between experiments and with the natural prototype. Compare with Figs. 5 to 10. Red arrows in the natural prototype are tectonic rotations from characteristic remanent magnetizations (Maffione et al., 2010; Poblete et al., 2014). Shortening magnitudes, orientations and the type and orientation of faults in the natural prototype are the same as in Fig. 1. (For interpretation of the references to color in this figure legend, the reader is referred to the web version of this article.)

Arc, which indicate an approximately north-moving Fuegian Backstop during the Paleogene–Miocene (cf. Torres Carbonell et al., 2014). An end member for this situation would be represented by experiment 3, in which the northward push was more important and rotation would be limited to a prior stage (e.g. Late Cretaceous). However, the N-directed movement involves an amount of right-lateral oblique-slip in the western limb which has no analog in the natural prototype.

6. Conclusions

Using analog modeling, we appraised different tectonic models of the Patagonian curve, considering the role of the rigid basement subsurface geometry in the foreland deformation. We focused our attention on the structural evolution of the curve segment representing the Fuegian thrust–fold belt in the experiments, and compared the experimental results with the structural geology of this portion of the southernmost Andes.

All our experiments conspicuously reproduce the buttressing effect of the Río Chico Arch promontory on the location and geometry of the thrust front, as was proposed in previous work as a fundamental control on the development of the orogenic curve. In the performed models this effect seems to be independent of the initial form and further kinematic evolution of the backstop.

Our experiments also show that a rectilinear backstop pushing in a northeastward direction is not capable of reproducing the type of shortening gradients, shortening directions and fault types recognized along the curved Fuegian thrust–fold belt. On the other hand, an originally curved backstop adequately reproduces the higher deformation in the apex of the curve, such as the higher shortenings registered in the apex of the Península Mitre Recess in Tierra del Fuego. However, only with simultaneous rotation during push it is possible to obtain movement of thrust sheets toward the rigid foreland obstacle, i.e. with a convergent motion. This kind of motion allows the shortening directions to be highly oblique to the thrust front along the complete sand wedge, including in particular NNW–SSE shortenings in the eastern part of the wedge. On the contrary, a fixed curved backstop moving in a single direction (i.e. north or NE) inevitably causes segments of the wedge to be affected by dominant strike-slip or oblique faulting.

Even though the available data on characteristic remanent magnetizations is not abundant, our experiments give some constraints on the predicted rotational behavior of an orogenic curve being progressively formed by collision against a basement promontory. Rotation of the backstop seems to control the extent of CCW rotations along the sand wedge, which were observed in the whole wedge segments in front of the rotational parts of the backstop. For the models without backstop rotation, the initial shape of the backstop and the presence of the rigid obstacle controlled the shape of the fault surfaces, which were born curved. Fault curvature caused an obliquity of fault slips and consequent rotation limited to the oblique fault zones. The sand wedge, however, did not rotate as a whole in these experiments.

In summary our results highlight the significance of the interaction with the backstop and promontory for the final configuration of the thrust wedge. These two factors should therefore be considered in any complete tectonic model of the Patagonian curve.

Acknowledgements

We acknowledge financial support from ANPCYT-FONCYT PICT 2012-2495, PICT 2011-0166, PICT 2012-2176, PICT 2010-1441; CONICET PIP 2011-0390; and SECyT-UNS Pgi 24/H117. The provision of an academic license from Midland Valley for the Move software (version 2014.2) is greatly appreciated. Reviews by F. Storti (Università Degli Studi di Parma), P. Cobbold (Univ. of Rennes), and M. Bonini (Inst. of Geosciences and Earth Resources, Florence), as well as Editor J-P. Avouac, improved our manuscript and are therefore greatly appreciated.

References

Adam, J., Urai, J.L., Wieneke, B., Oncken, O., Pfeiffer, K., Kukowski, N., Lohrmann, J., Hoth, S., van der Zee, W., Schmatz, J., 2005. Shear localisation and strain distribution during tectonic faulting—new insights from granular-flow experiments and high-resolution optical image correlation techniques. J. Struct. Geol. 27, 283–301.

Alvarez-Marrón, J., McClay, K., Harambour, S., Rojas, L., Skarmeta, J., 1993. Geometry and evolution of the frontal part of the Magallanes foreland thrust and fold belt (Vicuña Area), Tierra del Fuego, Southern Chile. AAPG Bull. 77, 1904–1921.

Barker, P.F., 2001. Scotia Sea regional tectonic evolution: implications for mantle flow and palaeocirculation. Earth Sci. Rev. 55, 1–39.

Biddle, K., Uliana, M., Mitchum Jr., R., Fitzgerald, M., Wright, R., 1986. In: Allen, P.A., Homewood, P. (Eds.), The Stratigraphic and Structural Evolution of the Central and Eastern Magallanes Basin, Southern South America. International Association of Sedimentologists Special Publication, Foreland Basins, pp. 41–66.

Bonini, M., Sokoutis, D., Talbot, C.J., Boccaletti, M., Milnes, A.G., 1999. Indenter growth in analogue models of Alpine-type deformation. Tectonics 18, 119–128.

Bonini, M., Sokoutis, D., Mulugeta, G., Katrivanos, E., 2000. Modelling hanging wall accommodation above rigid thrust ramps. J. Struct. Geol. 22, 1165–1179.

Bruhn, R.L., 1979. Rock structures formed during back-arc basin deformation in the Andes of Tierra del Fuego. Geol. Soc. Am. Bull. 90, 998–1012.

Burns, K.L., Rickard, M.J., Belbin, L., Chamalaun, F., 1980. Further palaeomagnetic confirmation of the magellanes orocline. Tectonophysics 63, 75–90.

Byerlee, J., 1978. Friction of rocks. Pure Appl. Geophys. 116, 615–626.

Calderón, M., Fildani, A., Hervé, F., Fanning, C.M., Weislogel, A., Cordani, U., 2007. Late Jurassic bimodal magmatism in the northern sea-floor remnant of the Rocas Verdes basin, southern Patagonian Andes. J. Geol. Soc. Lond. 164, 1011–1022.

Cao, S.J., Torres Carbonell, P.J., Frisicale, M.C., Dimieri, L.V., 2015. Evidencias meso y microestructurales de una faja milonítica regional en el Monte Olivia, Tierra del Fuego: implicancias para la evolución tectónica de los Andes Fueguinos. XVI Reunión de Tectónica 19–23 October 2015, General Roca, Argentina.

Carey, S., 1958. A tectonic approach to continental drift. In: Carey, S. (Ed.), Continental Drift: a Symposium. Univ. of Tasmania, Hobart, Australia, pp. 177–355.

Cunningham, D.W., 1993. Strike-slip faults in the Southernmost Andes and the development of the Patagonian Orocline. Tectonics 12, 169–186.

Cunningham, W.D., Klepeis, K.A., Gose, W.A., Dalziel, I.W.D., 1991. The Patagonian Orocline: new paleomagnetic data from the Andean Magmatic Arc in Tierra del Fuego, Chile. J. Geophys. Res. 96, 16061–16067.

Dalziel, I., Kligfield, R., Lowrie, W., Opdyke, N., 1973. Paleomagnetic data from the southernmost Andes and the Antarctandes. In: Tarling, D.H., Runcorn, S.K. (Eds.), Implications of Continental Drift to the Earth Sciences. Academic Press, London, pp. 87–101.

Dalziel, I.W.D., 1986. Collision and Cordilleran orogenesis: an Andean perspective. Geol. Soc. Lond., Spec. Publ. 19, 389–404.

Dalziel, I.W.D., Lawver, L.A., Norton, I.O., Gahagan, L.M., 2013a. The Scotia Arc: genesis, evolution, global significance. Annu. Rev. Earth Planet. Sci. 41, 767–793.

Dalziel, I.W.D., Lawver, L.A., Pearce, J.A., Barker, P.F., Hastie, A.R., Barfod, D.N., Schenke, H.-W., Davis, M.B., 2013b. A potential barrier to deep Antarctic circumpolar flow until the late Miocene? Geology 41, 947–950. http://dx.doi.org/10.1130/G34352.1.

Davis, D., Suppe, J., Dahlen, F.A., 1983. Mechanics of fold and thrust belts and accretionary wedges. J. Geophys. Res. 88, 1153–1172.

Diraison, M., Cobbold, P., Gapais, D., Rossello, E., Le Corre, C., 2000. Cenozoic crustal thickening, wrenching and rifting in the foothills of the southernmost Andes. Tectonophysics 316, 91–119.

Fildani, A., Hessler, A.M., 2005. Stratigraphic record across a retroarc basin inversion: Rocas Verdes-Magallanes Basin, Patagonian Andes, Chile. Geol. Soc. Am. Bull. 117, 1596–1614.

Fosdick, J.C., Romans, B.W., Fildani, A., Bernhardt, A., Calderón, M., Graham, S.A., 2011. Kinematic Evolution of the Patagonian Retroarc Fold-And-Thrust Belt and Magallanes Foreland Basin, Chile and Argentina, 51°30'S. Geological Society of America Bulletin.

Galeazzi, J.S., 1998. Structural and stratigraphic evolution of the western Malvinas Basin, Argentina. AAPG Bull. 82, 596–636.

Ghiglione, M.C., Cristallini, E.O., 2007. Have the southernmost Andes been curved since Late Cretaceous time? An analog test for the Patagonian Orocline. Geology 35, 13–16.

Ghiglione, M.C., Quinteros, J., Yagupsky, D., Bonillo-Martínez, P., Hlebszevtich, J., Ramos, V.A., Vergani, G., Figueroa, D., Quesada, S., Zapata, T., 2010. Structure and tectonic history of the foreland basins of southernmost South America. J. S. Am. Earth Sci. 29, 262–277.

Ghiglione, M.C., Suarez, F., Ambrosio, A., Da Poian, G., Cristallini, E.O., Pizzio, M.F., Reinoso, R.M., 2009. Structure and evolution of the austral basin fold-thrust belt, Southern Patagonian Andes. Rev. Asoc. Geol. Argent. 65, 215–226.

Gomes, C., Pereira-Filho, M., Braga, S., 2003. Experimental models of 'Basement'-controlled salients — application to the Proterozoic fold-thrust belt of the Quadrilátero Ferrífero (Minas Gerais, Southeastern Brazil). An. Acad. Bras. Cienc. 75, 249–263.

Gutscher, M.-A., Kukowski, N., Malavieille, J., Lallemand, S., 1996. Cyclical behavior of thrust wedges: insights from high basal friction sandbox experiments. Geology 24, 135–138.

Hubbert, M., 1937. Theory of scaled models as applied to the study of geological structures. Geol. Soc. Am. Bull. 48, 1459–1520.

Hubbert, M., 1951. Mechanical basis for certain familiar geologic structures. Geol. Soc. Am. Bull. 62, 355–372.

Klepeis, K.A., 1994. The Magallanes and Deseado fault zones: major segments of the South American–Scotia transform plate boundary in southernmost South America, Tierra del Fuego. J. Geophys. Res. 99, 22001–22014.

Klepeis, K.A., Betka, P., Clarke, G., Fanning, M., Hervé, F., Rojas, L., Mpodozis, C., Thomson, S., 2010. Continental underthrusting and obduction during the Cretaceous closure of the Rocas Verdes rift basin, Cordillera Darwin, Patagonian Andes. Tectonics 29, TC3014.

Kley, J., Monaldi, C.R., Salfity, J.A., 1999. Along-strike segmentation of the Andean foreland: causes and consequences. Tectonophysics 301, 75–94.

Kohn, M.J., Spear, F.S., Dalziel, I.W.D., 1993. Metamorphic P–T Paths from Cordillera Darwin, a core complex in Tierra del Fuego, Chile. J. Petrol. 34, 519–542.

Konstantinovskaya, E., Malavieille, J., 2011. Thrust wedges with décollement levels and syntectonic erosion: a view from analog models. Tectonophysics 502, 336–350. http://dx.doi.org/10.1016/j.tecto.2011.01.020.

Koyi, H., 1995. Mode of internal deformation in sand wedges. J. Struct. Geol. 17, 293–300.

Koyi, H.A., Maillot, B., 2007. Tectonic thickening of hanging-wall units over a ramp. J. Struct. Geol. 29, 924–932.

Kraemer, P.E., 2003. Orogenic shortening and the origin of the Patagonian orocline (56° S.Lat). J. S. Am. Earth Sci. 15, 731–748.

Krantz, R., 1991. Measurements of friction coefficients and cohesion for faulting and fault reactivation in laboratory models using sand and sand mixture. Tectonophysics 188, 203–207.

Lickorish, W.H., Ford, M., Bürgisser, J., Cobbold, P.R., 2002. Arcuate thrust systems in sandbox experiments: a comparison to the external arcs of the Western Alps. Geol. Soc. Am. Bull. 114, 1089–1107.

Liu, H., McClay, K., Powell, D., 1992. Physical models of thrust wedges. In: McClay, K. (Ed.), Thrust Tectonics. Chapman and Hall, London, pp. 71–81.

Lodolo, E., Menichetti, M., Bartole, R., Ben-Avraham, Z., Tassone, A., Lippai, H., 2003. Magallanes–Fagnano continental transform fault (Tierra del Fuego, southernmost South America). Tectonics 22.

Macedo, J., Marshak, S., 1999. Controls on the geometry of fold-thrust belt salients. Geol. Soc. Am. Bull. 111, 1808–1822.

Maestro, A., Ruano, P., Torres Carbonell, P., Bohoyo, F., Galindo-Zaldívar, J., Pedrera, A., Ruíz-Constán, A., González-Castillo, L., Ibarra, P., López-Martínez, J., 2015. Paleostress fields in Tierra del Fuego and their relationship with the Scotia Arc based on brittle mesostructure population analysis. XII International Symposium on Antarctic Earth Sciences 13–17 July 2015, Goa, India. Abstracts, 232.

Maffione, M., Speranza, F., Faccenna, C., Rossello, E., 2010. Paleomagnetic evidence for a pre-early Eocene (~50 Ma) bending of the Patagonian orocline (Tierra del Fuego, Argentina): paleogeographic and tectonic implications. Earth Planet. Sci. Lett. 289, 273–286.

Malavieille, J., 1984. Modélisation expérimentale des chevauchements imbriqués; application aux chaînes de montagnes. Bulletin de la Société Géologique de France 26, 129–138.

Marshak, S., 2004. Salients, recesses, arcs, oroclines, and syntaxes—a review of ideas concerning the formation of map-view curves in fold-thrust belts. In: McClay, K.R. (Ed.), Thrust tectonics and hydrocarbon systems: AAPG Memoir. American Association of Petroleum Geologists, pp. 131–156.

Mukasa, S.B., Dalziel, I.W.D., 1996. Southernmost Andes and South Georgia Island, North Scotia Ridge: zircon U–Pb and muscovite 40Ar39Ar age constraints on tectonic evolution of Southwestern Gondwanaland. J. S. Am. Earth Sci. 9, 349–365.

Nelson, E.P., Dalziel, I.W.D., Milnes, A.G., 1980. Structural geology of the Cordillera Darwin — collisional-style orogenesis in the southernmost Chilean Andes. Eclogae Geol. Helv. 73, 727–751.

Olivero, E.B., Malumián, N., 2008. Mesozoic-Cenozoic stratigraphy of the Fuegian Andes, Argentina. Geol. Acta 6, 5–18.
Olivero, E.B., Martinioni, D.R., 2001. A review of the geology of the Argentinian Fuegian Andes. J. S. Am. Earth Sci. 14, 175–188.
Panza, J., Sacomani, L., Cobos, J., 2002. Mapa geológico de la Provincia de Santa Cruz. Servicio Geológico y Minero de Argentina Buenos Aires, Argentina.
Poblete, F., Roperch, P., Hervé, F., Diraison, M., Espinoza, M., Arriagada, C., 2014. The curved Magallanes fold and thrust belt: tectonic insights from a paleomagnetic and anisotropy of magnetic susceptibility study. Tectonics 33 2014TC003555.
Poblete, F., Roperch, P., Hervé, F., Ramírez, C., Arriagada, C., 2013. On the possibility and timing for tectonic rotations in Patagonia: new paleomagnetic and AMS data from southernmost South America. In: Charrier, R.e.a. (Ed.), GeoSur 2013, International Geological Congress on the Southern Hemisphere. Bollettino di Geofisica Teorica ed Applicata, Viña del Mar, Chile, pp. 306–307.
Ponce, J.J., Olivero, E.B., Martinioni, D.R., 2008. Upper Oligocene–Miocene clinoforms of the foreland Austral Basin of Tierra del Fuego, Argentina: stratigraphy, depositional sequences and architecture of the foredeep deposits. J. S. Am. Earth Sci. 26, 36–54.
Rapalini, A.E., 2007. A paleomagnetic analysis of the Patagonian orocline. Geol. Acta 5, 287–294.
Robbiano, J.A., Arbe, H.A., Gangui, A., 1996. Cuenca Austral Marina. In: Ramos, V.A., Turic, M.A. (Eds.), Geología y recursos naturales de la Plataforma Continental Argentina, Relatorio del XIII° Congreso Geológico Argentino y III° Congreso de Exploración de Hidrocarburos. Asociación Geológica Argentina. Instituto Argentino del Petróleo, Buenos Aires, pp. 323–341.
Sanford, A.R., 1959. Analytical and experimental study of simple geologic structures. Geol. Soc. Am. Bull. 70, 19–52.
SERNAGEOMIN, 2003. Mapa Geológico de Chile. Servicio Nacional de Geología y Minería. Santiago, Chile.
Storti, F., Salvini, F., McClay, K., 2000. Synchronous and velocity-partitioned thrusting and thrust polarity reversal in experimentally produced, doubly-vergent thrust wedges: implications for natural orogens. Tectonics 19, 378–396.
Sveen, J., 2004. An Introduction to MatPIV v. 1.6.1. User Reference Manual.
Tanner, P.W.G., Macdonald, D.I.M., 1982. Models for the deposition and simple shear deformation of a turbidite sequence in the South Georgia portion of the southern Andes back-arc basin. J. Geol. Soc. 139, 739–754.
Torres Carbonell, P.J., Dimieri, L.V., 2013. Cenozoic contractional tectonics in the Fuegian Andes, southernmost South America: a model for the transference of orogenic shortening to the foreland. Geol. Acta 11, 359–370.
Torres Carbonell, P.J., Dimieri, L.V., Martinioni, D.R., 2013b. Early foreland deformation of the Fuegian Andes (Argentina): constraints from the strain analysis of Upper Cretaceous–Danian sedimentary rocks. J. Struct. Geol. 48, 14–32.
Torres Carbonell, P.J., Dimieri, L.V., Olivero, E.B., 2011. Progressive deformation of a Coulomb thrust wedge: the eastern Fuegian Andes thrust–fold Belt. In: Poblet, J., Lisle, R. (Eds.), Kinematic Evolution and Structural Styles of Fold-and-Thrust Belts, Geological Society, London. Special Publications. The Geological Society, Bath, pp. 123–147.
Torres Carbonell, P.J., Dimieri, L.V., Olivero, E.B., 2013a. Evaluation of strain and structural style variations along the strike of the Fuegian thrust–fold belt front, Argentina. Andean Geology 40, 438–457.
Torres Carbonell, P.J., Dimieri, L.V., Olivero, E.B., Bohoyo, F., Galindo-Zaldívar, J., 2014. Structure and tectonic evolution of the Fuegian Andes (southernmost South America) in the framework of the Scotia Arc development. Global Planet. Change 123 (Part B), 174–188.
Torres Carbonell, P.J., Olivero, E.B., Dimieri, L.V., 2008a. Control en la magnitud de desplazamiento de rumbo del Sistema Transformante Fagnano, Tierra del Fuego, Argentina. Revista Geológica de Chile 35, 63–77.
Torres Carbonell, P.J., Olivero, E.B., Dimieri, L.V., 2008b. Structure and evolution of the Fuegian Andes foreland thrust–fold belt, Tierra del Fuego, Argentina: paleogeographic implications. J. S. Am. Earth Sci. 25, 417–439.
White, D., Take, W., Bolton, M., 2001. Measuring soil deformation in geotechnical models using digital images and PIV analysis. 10th International Conference on Computer Methods and Advances in Geomechanics. Tucson, AZ.
Wilson, T.J., 1991. Transition from back-arc to foreland basin development in the southernmost Andes: stratigraphic record from the Ultima Esperanza District, Chile. Geol. Soc. Am. Bull. 103, 98–111.
Wolf, H., König, D., Triantafyllidis, T., 2003. Experimental investigation of shear band patterns in granular material. J. Struct. Geol. 25, 1229–1240.
Yagupsky, D., 2010. Metodología para el estudio de sistemas compresivos y de sus controles estucturales. Facultad de Ciencias Exactas y Naturales. Universidad de Buenos Aires, Buenos Aires, p. 203.
Yrigoyen, M., 1989. Cuenca de Malvinas. In: Chebli, G.A., Spalletti, L.A. (Eds.), Cuencas Sedimentarias Argentinas. Serie Correlación Geológica. Universidad Nacional de Tucumán, Instituto Superior de Correlación Geológica, Tucumán, pp. 481–491.
Zanella, A., Cobbold, P.R., Rojas, L., 2014. Beef veins and thrust detachments in Early Cretaceous source rocks, foothills of MagallanesAustral Basin, southern Chile and Argentina: structural evidence for fluid overpressure during hydrocarbon maturation. Mar. Pet. Geol. 55, 250–261. http://dx.doi.org/10.1016/j.marpetgeo.2013.10.006.